JOURNAL OF PETROLOGY | VOLUME 51 | NUMBER 8 | PAGES 1711–1738 | 2010 | doi:10.1093/petrology/egq036

Mantle Melting as a Function of Water Content beneath the Mariana Arc

KATHERINE A. KELLEY[1]*, TERRY PLANK[2], SALLY NEWMAN[3], EDWARD M. STOLPER[3], TIMOTHY L. GROVE[4], STEPHEN PARMAN[5] AND ERIK H. HAURI[6]

[1]GRADUATE SCHOOL OF OCEANOGRAPHY, UNIVERSITY OF RHODE ISLAND, NARRAGANSETT BAY CAMPUS, NARRAGANSETT, RI 02882, USA

[2]LAMONT–DOHERTY EARTH OBSERVATORY, COLUMBIA UNIVERSITY, PALISADES, NY 10964, USA

[3]DIVISION OF GEOLOGICAL AND PLANETARY SCIENCES, CALIFORNIA INSTITUTE OF TECHNOLOGY, PASADENA, CA 91125, USA

[4]DEPARTMENT OF EARTH, ATMOSPHERIC, AND PLANETARY SCIENCES, MASSACHUSETTS INSTITUTE OF TECHNOLOGY, CAMBRIDGE, MA 02142, USA

[5]DEPARTMENT OF GEOLOGICAL SCIENCES, BROWN UNIVERSITY, PROVIDENCE, RI 02912, USA

[6]DEPARTMENT OF TERRESTRIAL MAGNETISM, CARNEGIE INSTITUTION OF WASHINGTON, 5241 BROAD BRANCH ROAD NW, WASHINGTON, DC 20015, USA

RECEIVED DECEMBER 4, 2009; ACCEPTED JUNE 10, 2010
ADVANCE ACCESS PUBLICATION JULY 3, 2010

Subduction zone magmas are characterized by high concentrations of pre-eruptive H_2O, presumably as a result of an H_2O flux originating from the dehydrating, subducting slab. The extent of mantle melting increases as a function of increasing water content beneath back-arc basins and is predicted to increase in a similar manner beneath arc volcanoes. Here, we present new data for olivine-hosted, basaltic melt inclusions from the Mariana arc that reveal pre-eruptive H_2O contents of ~1·5–6·0 wt %, which are up to three times higher than concentrations reported for the Mariana Trough back-arc basin. Major element systematics of arc and back-arc basin basalts indicate that the back-arc basin melting regime does not simply mix with wet, arc-derived melts to produce the observed range of back-arc magmatic H_2O concentrations. Simple melting models reveal that the trend of increasing extents of melting with increasing H_2O concentrations of the mantle source identified in the Mariana Trough generally extends beneath the Mariana volcanic front to higher mantle water contents and higher extents of melting. In detail, however, each Mariana volcano may define a distinct relationship between extent of melting and the H_2O content of the mantle source. We develop a revised parameterization of hydrous melting, incorporating terms for variable pressure and mantle fertility, to describe the distinct relationships shown by each arc volcano. This model is used in combination with thermobarometry constraints to show that hydrous melts equilibrate at greater depths (34–87 km) and temperatures (>1300°C) beneath the Mariana arc than beneath the back-arc basin (21–37 km), although both magma types can form from a mantle of similar potential temperature (~1350°C). The difference lies in where the melts form and equilibrate. Arc melts are dominated by those that equilibrate within the hot core of the mantle wedge, whereas back-arc melts are dominated by those that equilibrate within the shallow zone of decompression melting beneath the spreading center. Despite higher absolute melting temperatures (>1300°C), Mariana arc melts reflect lower melt productivity as a result of wet melting conditions and a more refractory mantle source.

KEY WORDS: *subduction; mantle melting; melt inclusions; magmatic volatiles*

*Corresponding author. Telephone: (401) 874-6838. Fax: (401) 874-6811. E-mail: kelley@gso.uri.edu

INTRODUCTION

Water plays a central role in subduction zone magmatism. Driven from the subducting plate during metamorphic dehydration, water enters and modifies the mantle wedge beneath arc volcanoes. The well-established effect of water in lowering the peridotite solidus (e.g. Kushiro *et al.*, 1968; Gaetani & Grove, 1998; Grove *et al.*, 2006; Hirschmann *et al.*, 2009) is thought to be a principal cause of mantle wedge melting, which is ultimately expressed as volcanism at the surface. Arc lavas show characteristic enrichments in fluid-mobile trace elements that are believed to participate, along with water, in these mass transfer and melting processes (e.g. Tera *et al.*, 1986; Morris *et al.*, 1990; Plank & Langmuir, 1993; Elliott *et al.*, 1997); however, the development of direct, quantitative relationships between H_2O and key subduction zone processes in natural systems has been slow.

Water contents of magmas have until recently been difficult to measure in arc systems because subaerially erupted lava degasses at low pressures, releasing most of the volatiles (e.g. H_2O, CO_2, S) that were dissolved in the liquid phase of the magma at high pressure. Melt inclusions, however, preserved as blebs of glass trapped in phenocrysts, often retain the pre-eruptive, dissolved volatiles that are lost from the bulk lava during degassing because they typically form when the magma was at depth. Enclosed within their crystalline containers, such inclusions were never exposed to low pressures on eruption. These tiny inclusions thus provide a means of bypassing the problem of volatile loss from conventional, whole-rock samples or from matrix glasses. Early evidence for high magmatic water contents in arc melt inclusions was found by Anderson (e.g. Anderson, 1979, 1982), who used the difference of the sum of major element oxides from 100% in glass inclusions from arc volcanoes to infer high dissolved H_2O concentrations (2–7 wt %). Recent innovations in microbeam analytical techniques such as Fourier transform infrared spectrometry (FTIR) and secondary ionization mass spectrometry (SIMS) have since established and streamlined the direct micro-analysis of volatiles in glasses (e.g. Stolper, 1982; Sisson & Layne, 1993; Sobolev & Chaussidon, 1996; Hauri, 2002*a*). Now, a rapidly growing database of direct measurements and experimental predictions of high H_2O contents in arc magmas has shown Anderson's original inferences to have been correct (e.g. Sisson & Grove, 1993*b*; Newman *et al.*, 2000; Grove *et al.*, 2002; Wallace, 2005), and current work continues to demonstrate the tremendous utility of igneous melt inclusions as messengers of deep magmatic and mantle processes (e.g. Sobolev & Shimizu, 1993; Nielsen *et al.*, 1995; Sobolev & Chaussidon, 1996; Saal *et al.*, 1998, 2002; Baker *et al.*, 2005; Baker, 2008; Johnson *et al.*, 2009).

A number of recent studies have investigated the pre-eruptive water contents of arc magmas using melt inclusion or glass data and experimental techniques, drawing important links between magmatic H_2O and arc volcanic processes (e.g. Roggensack *et al.*, 1997; Roggensack, 2001; Blundy *et al.*, 2006), the bulk composition of arc magmas (e.g. Sisson & Grove, 1993*a*, 1993*b*; Grove *et al.*, 2002; Gaetani & Grove, 2003; Wood, 2004) and fluid-mobile trace element signatures (e.g. Cervantes & Wallace, 2003; Sadofsky *et al.*, 2008). Several studies have specifically examined the relationship between magmatic water concentrations and indicators of the extent of mantle melting in subduction zone settings. Stolper & Newman (1994) used natural pillow glass samples from the Mariana Trough back-arc basin to model a direct relationship between water content and the extent of mantle melting, as evidenced by the correlation of increasing magmatic H_2O with decreasing TiO_2. A number of studies have since supported and built upon these observations and models, using additional data for the Mariana Trough and other global back-arc basins (e.g. Gribble *et al.*, 1996, 1998; Kelley *et al.*, 2006; Langmuir *et al.*, 2006), all in support of the paradigm that high water contents in the source regions beneath back-arc basins lead both to high overall extents of mantle melting beneath back-arc basins and elevated dissolved H_2O contents in the resulting partial melts. Some recent work has also drawn similar links between melting processes and high magmatic H_2O at arc volcanoes using minor and trace elements as proxies for melt fraction (e.g. Walker *et al.*, 2003; Portnyagin *et al.*, 2007; Johnson *et al.*, 2009). Nevetheless, although geochemical data suggest a causal relationship between water flux and extent of mantle melting beneath arcs and back-arc basins, the connections between these two types of wet melting systems have not been fully developed.

Recent work has begun to forge a framework for realistic models of melting processes and melt transport in the mantle wedge. For example, models involving reactive transport of water (e.g. Davies & Stevenson, 1992) or reactive porous flow of melt through the wedge interior (e.g. Kelemen *et al.*, 2003; Grove *et al.*, 2006), mixing of melts from distinctly separate wet and dry melting regimes (e.g. Langmuir *et al.*, 2006), and buoyant, coincident ascent of hydrated mantle plus melt (e.g. Hall & Kincaid, 2001; Gerya & Yuen, 2003; Kelley *et al.*, 2006) have all been proposed to explain the observed range of melt compositions in specific arc and back-arc basin settings. Despite this progress, we still lack quantitative treatments that link these processes with the water flux from the subducting plate. Cross-arc traverses of subaerial volcanism in Guatemala, Kamchatka, and Mexico (Walker *et al.*, 2003; Portnyagin *et al.*, 2007; Johnson *et al.*, 2009) suggest that the role of water in magma production generally diminishes with distance behind the volcanic front. This idea is supported by observations of back-arc basin basalts, which display an overall global decrease in magmatic

water content with distance from the trench (e.g. Kelley *et al.*, 2006).

The premise of this study is to develop a broader understanding of the links and distinctions between arc and back-arc melting processes and how these relate to the behavior of water in the mantle source. We will show that this is possible based on several recent, comprehensive studies of back-arc basin magmatism (e.g. Taylor & Martinez, 2003; Kelley *et al.*, 2006; Langmuir *et al.*, 2006; Wiens *et al.*, 2010), which permit both the sub-arc flux melting process and the role of related processes in back-arc basin magmatism to be compared for a single arc–back-arc basin pair such as the Marianas. In addition to using literature data in our analysis, we present new combined major element and volatile data for olivine-hosted glass inclusions from four islands of the Mariana arc. These data are then used to (1) evaluate the conditions and processes driving mantle melting beneath arcs, (2) explore how recent models of back-arc basin melting processes relate to processes beneath the Mariana arc, and (3) assess the relationship between the arc and back-arc melting regimes in the Mariana system. The melting processes in these systems are ultimately reflective of important contrasts in the shape of the geotherm, the fertility of the mantle wedge, and the amount of H_2O added to the mantle wedge.

SAMPLES AND METHODS

Mariana Arc scoria samples

The glass inclusions analyzed for this study come from seven Mariana arc scoria samples provided by A. T. Anderson, some of which provided the melt inclusions that were the focus of prior work (Anderson, 1982). These scoria samples originate from the Mariana islands of Guguan (GUG 79-1), Pagan (PB-14, PB-62, and PB-64), Agrigan (AGR19 and AGR-Kimi), and Sarigan (SA93), located in the central island province of the active Mariana arc (Fig. 1). Major and trace element analyses of whole-rock powders of these scoria samples are provided in Electronic Appendix 2 (downloadable from http://petrology.oxfordjournals.org/). From each scoria sample, we hand-picked olivine crystals from the available material, which came either as mineral separates that had been crushed, sieved, and separated using methylene iodide by Anderson or as bulk hand samples of centimeter-scale lapilli to fist-sized bombs that we then crushed and sieved. The olivine separates were immersed in mineral oil and examined under a binocular microscope to identify inclusion-bearing crystals. We selected only olivine-hosted inclusions consisting of clear, brown glass and petrographically determined to be fully enclosed within the host crystals (e.g. Fig. 2). Most of the studied inclusions contained a single vapor bubble and some inclusions contained co-entrained spinel crystals, determined to have been present syn-entrapment rather than crystallized post-entrapment because of their large sizes relative to the associated glass inclusions (see Electronic Appendix 3). In one rock in which naturally glassy inclusions were rare (AGR19), a subset of four crystallized inclusions were homogenized in a gas-mixing furnace for 10 min, following the technique of Hauri (2002*b*; see Table 1 and Electronic Appendix 3).

In addition to these new Mariana arc melt inclusion samples and data, we also incorporated data for olivine-hosted glass inclusions from these four Mariana islands from Shaw *et al.* (2008) in our dataset. Tephra samples yielding melt inclusions for the Shaw *et al.* (2008) study were collected during MARGINS-funded field expeditions to the Mariana islands in 2003–2004. Although their tephras are from the same islands as the samples examined in the present study, they are from different eruptive units. In detail, we expect that some samples from Shaw *et al.* (2008) may show compositional differences relative to the samples of the present study. We note that when subjected to the same screening criteria (see below), both sample sets give the same sense of variation in magmatic H_2O content (Pagan < Guguan < Agrigan), with the exception of Sarigan. The compositional contrast between the two Sarigan suites, however, is not surprising given that the samples are from different eruptions and could represent different magma batches.

Analytical methods

Glass inclusions were exposed and polished on a single side for electron microprobe analysis at the Massachusetts Institute of Technology (MIT). Major element, S, and Cl concentrations of the glasses (Table 1 and Electronic Appendix 3) were measured on the MIT JEOL Superprobe following the techniques outlined by Parman & Grove (2004) for hydrous glasses, using a beam defocused to 20 μm to minimize alkali loss and calibrating against the hydrous glass reference materials 1140mf#18 and 87s35a#14 (Sisson & Grove, 1993*b*). Major element compositions of the host olivine crystals were also measured by electron microprobe at either MIT or the Carnegie Institution of Washington (CIW). Host olivine crystals were also examined using backscattered electron (BSE) imaging to evaluate whether the hosts showed evidence of complex magmatic processes (e.g. reverse zoning, reaction textures, etc.); all host olivines were found to be either homogeneous or slightly normally zoned in forsterite content, reflecting simple magmatic histories. Volatile concentrations (H_2O and CO_2) in the glass inclusions were directly measured in one of two ways. Some inclusions were doubly intersected to make 30–100 μm thick wafers for analysis by FTIR at the California Institute of Technology, following the techniques of Newman *et al.* (2000; Table 1 and Electronic Appendix 3). Other inclusions were left with a single exposed side and

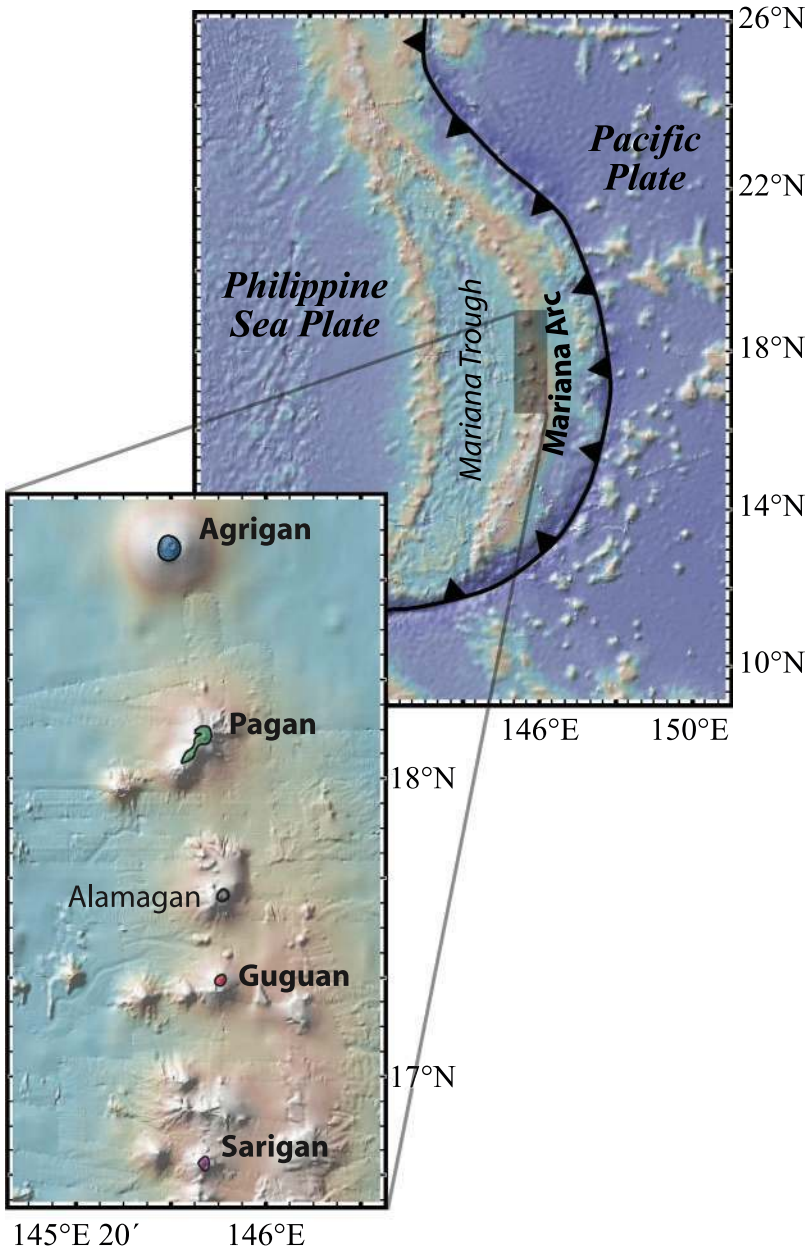

Fig. 1. Regional map of the Mariana subduction zone. The inset shows the locations of volcanoes (bold names) in the Mariana Central Island Province that provided the melt inclusion samples for this work.

the crystals were re-mounted in indium metal for volatile analysis (H_2O, CO_2, S, Cl, F) by ion microprobe at CIW using the procedures outlined by Hauri (2002*a*), using ^1H as the mass for determination of H_2O. One inclusion (AGR 19) was analyzed using both techniques and yielded agreement between the two methods of <2% relative (i.e. 5·00 wt % H_2O by FTIR vs 5·08 wt % H_2O by ion probe; Table 1 and Electronic Appendix 3).

DATA TREATMENT

Correction for post-entrapment crystallization

As a melt inclusion and crystal cool under magmatic conditions, olivine may precipitate from the melt onto the walls of its olivine container. We corrected for this post-entrapment crystallization (PEC) of olivine by adding equilibrium olivine [using $K_D^{ol-liq}(Fe^{2+}/Mg) = 0{\cdot}3$]

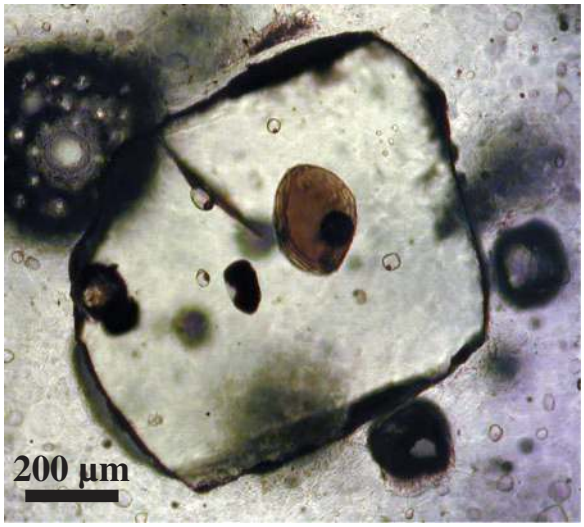

Fig. 2. Photomicrograph of an olivine-hosted melt inclusion. The inclusion pictured is sample GUG-D, from Guguan island. The olivine crystal is embedded in resin and has been polished to expose the melt inclusion at the surface. The inclusion is made of clear, brown glass and contains a single vapor bubble.

to each glass inclusion composition in 1% increments until the melt composition reached equilibrium with the forsterite content of a reference point in the host olivine measured ~40 μm from the inclusion interface. This correction is sensitive to the $Fe^{3+}/\Sigma Fe$ ratio (i.e. $Fe^{3+}/[Fe^{2+} + Fe^{3+}]$) of the melt. Although $Fe^{3+}/\Sigma Fe$ is unknown in these glass inclusions, we assume $Fe^{3+}/\Sigma Fe$ of 0·25 for all arc samples, which represents an average of $Fe^{3+}/\Sigma Fe$ ratios measured by micro-X-ray Absorption Near Edge Structure (XANES) spectroscopy for a separate suite of glass inclusions from sample GUG 79-1 (Kelley & Cottrell, 2009). These starting $Fe^{+3}/\Sigma Fe$ ratios are carried through all subsequent calculations, assuming the total moles of Fe^{3+} are conserved, which causes $Fe^{3+}/\Sigma Fe$ to decrease when olivine is added to the melt compositions. On average, the PEC correction requires <2·5% olivine added back to a given melt composition. To be conservative, any inclusions indicating >5% PEC of olivine were not used in the melting model. The compositions of the AGR19 inclusions that were homogenized in a 1 atm furnace as described above indicate that these inclusions resorbed 1–13% of the host olivine during the homogenization procedure. To correct for this, the composition of the host olivine was subtracted from each homogenized melt composition in 1% increments, using the same approach as described above to correct for crystallization on the inclusion wall, until the reconstructed melt was calculated to be in equilibrium with the host olivine. In rare instances, other minerals (e.g. clinopyroxene) also precipitated from the melt after entrapment as evidenced by BSE images from the electron microprobe. In cases where secondary or co-entrapped crystals were visible, we excluded those samples from further modeling, although we report the data in Electronic Appendix 3.

In some instances, post-entrapment processes may drive diffusional exchange of some elements (e.g. Fe) between the melt inclusion and the external magma. In the case of these Mariana arc melt inclusions, the results of Kelley & Cottrell (2009) rule out this potential complication. In their study, the $Fe^{3+}/\Sigma Fe$ of Guguan and Sarigan glass inclusions were measured directly by micro-XANES, and with these values, the Mariana inclusions are in near-perfect Fe–Mg exchange equilibrium with their olivine hosts. This indicates that post-entrapment Fe diffusion has not significantly modified the inclusion compositions.

Assessing the effects of degassing

Volatiles will partition into bubbles from the liquid component of magma as it decompresses on ascent and ultimately erupts. Despite the fact that melt inclusions are enclosed in crystalline hosts, they may trap melts after extensive degassing has already occurred, thus potentially compromising their utility as probes of the volatile contents of primitive melts and their mantle source regions, which is the goal of this study. Because of the differential solubilities of the various major volatile species, however, it is often possible to show that volatile loss was minimal and thus to ensure that the as-analyzed volatile contents of glass inclusions were not significantly affected by degassing during decompression. We evaluated the effects of degassing on the volatile contents of Mariana arc melt inclusions by examining the co-variation of volatile species (CO_2, S, H_2O). Of these, H_2O is the most soluble in basaltic magma at low pressure, and CO_2 is the least soluble (Dixon & Stolper, 1995); sulfur solubility in melt is a complex function of fO_2 and fS, but recent empirical observations of the relationship between S and the concentrations of other volatile species in arc melt inclusions suggest that its solubility may be between those of H_2O and CO_2 in basaltic arc magmas (e.g. Sisson & Layne, 1993; Wallace, 2005; Benjamin *et al.*, 2007). Degassing is thus expected to remove CO_2 from solution first, followed by S and H_2O.

The volatile data presented in Fig. 3 show the extent to which degassing may have removed these volatile species from Mariana arc glass inclusion compositions. Because of the low solubility of CO_2 relative to H_2O in silicate melt at low pressures, samples with >50 ppm CO_2 are considered to have retained enough CO_2 that H_2O is unlikely to have been significantly lost by degassing. Below 50 ppm CO_2, H_2O concentrations are more scattered and H_2O may or may not have significantly degassed (Fig. 3a). CO_2 may thus not be the most sensitive indicator of the overall effect of degassing on melt H_2O concentrations, and in cases where CO_2 is below detection by FTIR, which is a function of both CO_2 concentration and sample thickness,

Table 1: Major and volatile element compositions of primitive, undegassed Mariana arc melt inclusions and host olivines

Sample no.:		Agr19	Agr19C[1]	Agr19E[1]	Agr19F[1]	Gug#6b	GugA	GugC	GugD
Host rock:		AGR19	AGR19	AGR19	AGR19	GUG 79-1	GUG 79-1	GUG 79-1	GUG 79-1
Volcano:		Agrigan	Agrigan	Agrigan	Agrigan	Guguan	Guguan	Guguan	Guguan
Melt inclusion									
SiO_2	wt %	46·43	45·87	47·31	47·04	46·51	46·10	47·17	45·70
TiO_2	wt %	0·64	0·56	0·57	0·81	0·69	0·69	0·69	0·74
Al_2O_3	wt %	17·52	14·71	15·05	15·02	17·31	18·29	17·59	18·01
FeO*	wt %	10·18	13·07	12·04	12·67	11·03	11·21	11·19	11·32
Fe_2O_3†	wt %	2·83	3·63	3·35	3·52	3·06	3·11	3·11	3·15
FeO†	wt %	7·63	9·80	9·03	9·50	8·27	8·40	8·39	8·49
MnO	wt %	0·20	0·24	0·22	0·21	0·19	0·24	0·25	0·24
MgO	wt %	4·83	9·03	8·11	6·38	5·70	6·20	6·22	5·44
CaO	wt %	12·27	10·15	10·38	10·41	11·08	11·64	11·40	12·58
Na_2O	wt %	1·83	1·66	1·94	2·25	2·29	1·95	1·99	1·95
K_2O	wt %	0·59	0·23	0·29	0·45	0·38	0·21	0·33	0·30
P_2O_5	wt %	0·13	0·12	0·10	0·39	0·09	0·00	0·08	0·09
S[2]	ppm	1440	723	500	615	947		1644	1894
Cl[2]	ppm		580	705	934	895		647	678
H_2O[3]	wt %	5·00					3·26	3·80	3·28
CO_2[3]	ppm	260					—	—	—
H_2O[4]	wt %	5·08	4·69	3·88	3·99	2·92			
CO_2[4]	ppm	264	14	88		44			
S[4]	ppm	1380	973	575	860	1190			
Cl[4]	ppm	515	641	643	973				
F[4]	ppm	520	226	179	221	322			
$Fe^{3+}/\Sigma Fe$†		0·25	0·25	0·25	0·25	0·25	0·25	0·25	0·25
Host olivine									
SiO_2	wt %	39·32	39·75	39·90	39·83	39·24			
Al_2O_3	wt %	0·03	0·03	0·02	0·02	0·04			
FeO	wt %	17·99	18·33	18·40	19·34	19·45			
MnO	wt %								
MgO	wt %	42·12	41·75	41·38	40·86	40·64			
CaO	wt %	0·22	0·21	0·24	0·22	0·21			
NiO	wt %	0·06	0·02	0·02	0·05	0·07			
Total	wt %	99·73	100·09	99·97	100·32	99·66			
Fo		0·81	0·80	0·80	0·79	0·79			
PEC-corrected melt									
Olivine added	%	2	−13	-10	−1	0			
SiO_2	wt %	46·28	46·79	48·14	47·11	46·51	46·10	47·17	45·70
TiO_2	wt %	0·62	0·64	0·63	0·81	0·69	0·69	0·69	0·74
Al_2O_3	wt %	17·17	16·90	16·72	15·17	17·31	18·29	17·59	18·01
Fe_2O_3†	wt %	2·77	4·17	3·72	3·55	3·06	3·11	3·11	3·15
FeO	wt %	7·86	11·26	10·03	9·60	8·27	8·40	8·39	8·49
MnO	wt %	0·19	0·28	0·24	0·22	0·19	0·24	0·25	0·24
MgO	wt %	5·55	7·64	6·96	6·25	5·70	6·20	6·22	5·44
CaO	wt %	12·03	11·67	11·53	10·52	11·08	11·64	11·40	12·58
Na_2O	wt %	1·80	1·91	2·16	2·28	2·29	1·95	1·99	1·95
K_2O	wt %	0·58	0·27	0·32	0·46	0·38	0·21	0·33	0·30
P_2O_5	wt %	0·13	0·13	0·11	0·39	0·09	0·00	0·08	0·09
H_2O	wt %	4·98	5·40	4·31	4·03	2·92	3·26	3·80	3·28
CO_2	ppm	259	16	97	—	44	—	—	—
S	ppm	1353	1118	639	869	1190	2115	1644	1894
Cl	ppm	504	737	714	983		624	647	678
F	ppm	510	259	199	223	322			

(continued)

Table 1: Continued

Sample no.:		GugF	GugXa	GugAB-1	GugAE	PB14H	PB14Ka	PB14Kb	PB640-1A
Host rock:		GUG 79-1	GUG 79-1	GUG 79-1	GUG 79-1	PB14	PB14	PB14	PB64
Volcano:		Guguan	Guguan	Guguan	Guguan	Pagan	Pagan	Pagan	Pagan
Melt inclusion									
SiO_2	wt %	46·01	46·9	45·27	47·53	49·36	49·57	48·50	49·10
TiO_2	wt %	0·80	0·93	0·79	0·75	0·75	0·90	0·83	0·62
Al_2O_3	wt %	18·14	17·66	16·29	17·62	15·46	15·87	15·83	14·60
FeO*	wt %	11·80	10·65	13·14	10·92	11·27	11·03	11·49	11·13
Fe_2O_3†	wt %	3·28	2·96	3·65	3·03	3·13	3·06	3·19	3·09
FeO†	wt %	8·85	7·99	9·85	8·19	8·45	8·27	8·62	8·35
MnO	wt %	0·26	0·17	0·23	0·21	0·21	0·20	0·17	0·15
MgO	wt %	4·85	5·18	5·93	5·31	5·86	4·59	5·60	7·21
CaO	wt %	12·50	12·27	11·92	10·77	10·93	11·35	11·44	9·40
Na_2O	wt %	1·98	2·09	1·77	2·03	2·54	2·39	2·30	2·80
K_2O	wt %	0·33	0·23	0·33	0·31	0·51	0·48	0·44	0·59
P_2O_5	wt %	0·04	0·11	0·02	0·06	0·14	0·13	0·08	0·07
S^2	ppm	2001	901	1309	820	756	445	487	
Cl^2	ppm	763	841	988	898	477	610	620	
H_2O^3	wt %	3·25							2·90
CO_2^3	ppm	—							—
H_2O^4	wt %		3·18	4·49	3·03	2·28	2·52	2·35	
CO_2^4	ppm		18	60	42	19	16	31	
S^4	ppm		1247	1402	1105	810	613	592	
Cl^4	ppm		768	796	754	432	575	565	
F^4	ppm		213	203	197	216	240	241	
$Fe^{3+}/\sum Fe$†		0·25	0·25	0·25	0·25	0·25	0·25	0·25	0·25
Host olivine									
SiO_2	wt %	38·74	40·01	39·29		40·03	40·04	39·60	38·96
Al_2O_3	wt %	0·02	0·03	0·02		0·37	0·03	0·19	0·02
FeO	wt %	19·97	17·64	22·61		19·69	18·38	19·74	19·94
MnO	wt %								0·30
MgO	wt %	39·83	42·84	38·35		40·22	41·80	40·57	40·23
CaO	wt %	0·21	0·21	0·24		0·41	0·24	0·31	0·30
NiO	wt %	0·06	0·06	0·06		0·06	0·07	0·05	0·10
Total	wt %	98·84	100·79	100·57		100·78	100·56	100·45	99·85
Fo		0·78	0·81	0·75		0·78	0·80	0·79	0·78
PEC-corrected melt									
Olivine added	%	2	2	0		0	3	0	0
SiO_2	wt %	45·86	46·78	45·27	47·53	49·36	49·25	48·50	49·10
TiO_2	wt %	0·78	0·91	0·79	0·75	0·75	0·87	0·83	0·62
Al_2O_3	wt %	17·78	17·31	16·29	17·62	15·46	15·41	15·83	14·60
Fe_2O_3†	wt %	3·21	2·90	3·65	3·03	3·13	2·98	3·19	3·09
FeO	wt %	9·10	8·20	9·85	8·19	8·45	8·64	8·62	8·35
MnO	wt %	0·25	0·17	0·23	0·21	0·21	0·19	0·17	0·15
MgO	wt %	5·53	5·90	5·93	5·31	5·86	5·64	5·60	7·21
CaO	wt %	12·26	12·03	11·92	10·77	10·93	11·02	11·44	9·40
Na_2O	wt %	1·94	2·05	1·77	2·03	2·54	2·32	2·30	2·80
K_2O	wt %	0·32	0·22	0·33	0·31	0·51	0·46	0·44	0·59
P_2O_5	wt %	0·04	0·11	0·02	0·06	0·14	0·13	0·08	0·07
H_2O	wt %	3·19	3·11	4·49	3·03	2·28	2·45	2·35	2·90
CO_2	ppm		18	60	42	19	15	31	—
S	ppm	1962	1223	1402	1105	810	595	592	1419
Cl	ppm	748	753	796	754	432	559	565	716
F	ppm		209	203	197	216	233	241	

(continued)

Table 1: Continued

Sample no.:		PB640-2	PB64G	SA93B	SA93D
Host rock:		PB64	PB64	SA93	SA93
Volcano:		Pagan	Pagan	Sarigan	Sarigan
Melt inclusion					
SiO_2	wt %	49·71	49·5	49·51	51·17
TiO_2	wt %	0·74	0·56	1·01	0·90
Al_2O_3	wt %	14·95	15·45	16·57	15·99
FeO*	wt %	11·99	10·40	7·76	8·47
Fe_2O_3†	wt %	3·33	2·89	2·16	2·35
FeO†	wt %	8·99	7·80	5·82	6·35
MnO	wt %	0·18	0·16	0·14	0·18
MgO	wt %	7·27	7·17	4·59	4·91
CaO	wt %	9·46	9·58	11·89	10·14
Na_2O	wt %	2·27	2·96	2·34	2·70
K_2O	wt %	0·55	0·50	0·31	0·50
P_2O_5	wt %	0·04	0·00	0·02	0·08
S[2]	ppm		1652	1090	1172
Cl[2]	ppm		239	555	852
H_2O[3]	wt %	2·83	3·45		
CO_2[3]	ppm	—	123		
H_2O[4]	wt %			5·09	6·14
CO_2[4]	ppm			207	85
S[4]	ppm			1559	1378
Cl[4]	ppm			583	805
F[4]	ppm			265	362
$Fe^{3+}/\sum Fe$†		0·25	0·25	0·25	0·25
Host olivine					
SiO_2	wt %	37·86	39·39	40·99	39·97
Al_2O_3	wt %	0·03	0·02	0·12	0·02
FeO	wt %	20·31	17·98	14·55	16·38
MnO	wt %	0·29			
MgO	wt %	40·40	41·61	43·56	43·18
CaO	wt %	0·28	0·23	0·22	0·19
NiO	wt %	0·07	0·08	0·10	0·10
Total	wt %	99·26	99·30	99·54	99·83
Fo		0·78	0·80	0·84	0·82
PEC-corrected melt					
Olivine added	%	0	0	2	0
SiO_2	wt %	49·71	49·54	49·32	51·17
TiO_2	wt %	0·74	0·56	0·99	0·90
Al_2O_3	wt %	14·95	15·45	16·25	15·99
Fe_2O_3†	wt %	3·33	2·89	2·11	2·35
FeO	wt %	8·99	7·80	6·02	6·35
MnO	wt %	0·18	0·16	0·14	0·18
MgO	wt %	7·27	7·17	5·37	4·91
CaO	wt %	9·46	9·58	11·66	10·14
Na_2O	wt %	2·27	2·96	2·29	2·70
K_2O	wt %	0·55	0·50	0·30	0·50
P_2O_5	wt %	0·04	0·00	0·02	0·08
H_2O	wt %	2·83	3·45	4·99	6·14
CO_2	ppm	—	123	203	85
S	ppm	1464	1652	1529	1378
Cl	ppm	536	239	572	805
F	ppm			259	362

Major elements for melt inclusions and host olivines were determined by electron microprobe (EMP) at MIT. A subset of host olivines were analyzed by EMP at CIW. PEC-corrected melts have been corrected for post-entrapment crystallization of olivine following methods described in the text; volatile compositions used in this calculation are SIMS data where available, and otherwise are FTIR + EMP data.
*Total Fe reported as FeO.
†Fe_2O_3 calculated as 25% of total Fe prior to correction for post-entrapment crystallization.
[1]Crystallized inclusions re-homogenized in a gas-mixing furnace; compositions were corrected for excess olivine resorption by subtracting the host olivine composition from the melt as described in the text.
[2]Concentrations determined by EMP at MIT.
[3]Concentrations determined by FTIR at Caltech.
[4]Concentrations determined by SIMS at CIW.
—, concentration below the detection limit.

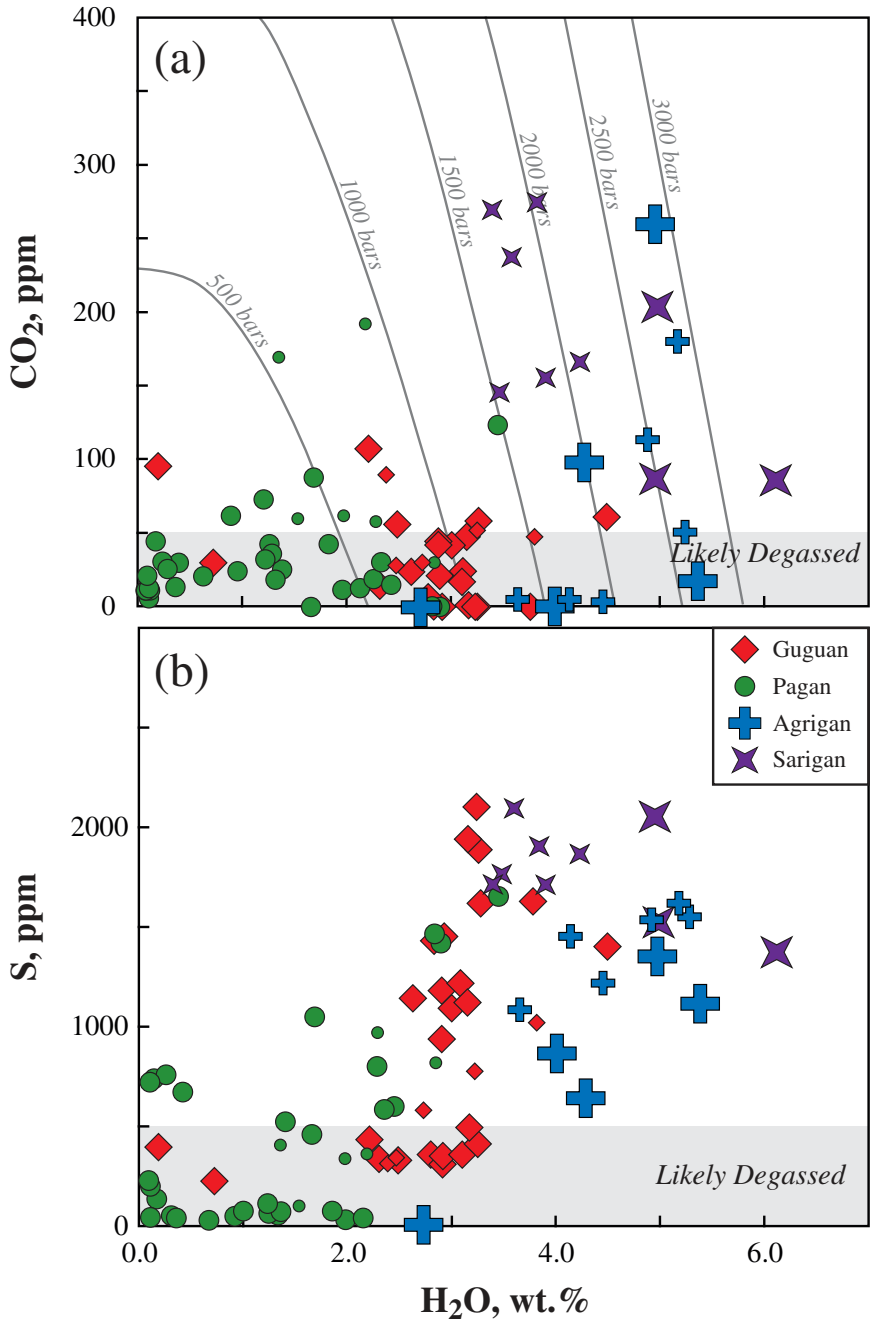

Fig. 3. Plot of volatile element concentrations, H_2O, CO_2 and S, in Mariana olivine-hosted melt inclusions. The larger symbols are data from this study; smaller symbols are data from Shaw *et al.* (2008). (a) H_2O vs CO_2. The shaded field identifies samples with 0–50 ppm CO_2, which are likely to have degassed some H_2O (see text). Isobars were calculated using the VolatileCalc vapor solubility model for basalt compositions (Newman & Lowenstern, 2002). (b) H_2O vs S. The shaded field identifies samples with 0–500 ppm S, which are likely to have degassed some H_2O (see text).

the extent of CO_2 degassing could not be determined. We also examined the relationship of H_2O to S in these melt inclusions, which appears to show more systematic co-variations within each suite of inclusions (Fig. 3b). Other studies have shown similar degassing systematics between S and H_2O (e.g. Sisson & Layne, 1993; Wade *et al.*, 2006; Benjamin *et al.*, 2007). We thus established a secondary filter at 500 ppm S, considering those inclusions with <500 ppm S to be degassed enough that H_2O may have been lost; the highest H_2O contents appear generally

consistent within each sample above this S concentration, and H_2O contents are more scattered below it.

Post-entrapment diffusion of H^+ could also potentially decouple melt H_2O concentrations from those of other, less soluble, volatiles. We note, however, that diffusive loss of H^+ from a melt inclusion would also result in significant oxidation of the inclusion as O^{2-} is left behind. Such a process would disrupt the Fe^{2+}–Mg exchange equilibrium between inclusions and their host olivines. As noted above, Mariana melt inclusions from these same samples are close to Fe^{2+}–Mg equilibrium with their host olivines, when measured $Fe^{3+}/\Sigma Fe$ ratios are accounted for, indicating that the redox conditions of the melt inclusions have not been significantly affected by H^+ diffusion (Kelley & Cottrell, 2009). There is thus no evidence that diffusive processes are the main cause of variability in H_2O content relative to other volatiles in these melt inclusions.

Assessing the effects of crystal fractionation

The PEC-corrected melt inclusions range in composition from basalt to basaltic andesite (~45–54 wt % SiO_2). Melt compositions from each Mariana island show major element variations consistent with synchronous degassing and fractional crystallization (Fig. 4). All inclusions identified as minimally degassed are relatively MgO-rich, with <51·2 wt % SiO_2 and >4·9 wt % MgO (Table 1 and Fig. 4a; note that glass inclusion data are plotted on an anhydrous basis in Fig. 4 for comparison with the whole-rock data), and generally have higher Al_2O_3 than degassed inclusions from the same islands (Fig. 4b). In Fig. 4b, however, the data suites for each island show distinct variations consistent with crystal fractionation. The point at which plagioclase saturation occurs, as indicated by the change from increasing to decreasing Al_2O_3 with decreasing MgO, is sensitive to magmatic H_2O content. Water suppresses plagioclase crystallization by stabilizing the Ab component in the melt (e.g. Yoder, 1969; Sisson & Grove, 1993*a*). The data for each island are consistent with plagioclase saturation at distinct magmatic H_2O concentrations, with the Pagan samples indicating earlier plagioclase saturation from a lower-H_2O melt, and the Agrigan samples consistent with late plagioclase saturation caused by high magmatic H_2O. These observations are supported by the measured H_2O concentrations of the most MgO-rich inclusions from each suite (filled symbols in Fig. 4), which are lowest at Pagan (average = 2·7 wt % H_2O) and highest at Agrigan (average = 4·5 wt % H_2O). This clear impact of water content on the liquid lines of descent of Mariana arc magmas has been developed as a magmatic hygrometer (Parman *et al.*, 2010).

Figure 4 identifies those melt inclusions that preserve the least fractionated compositions. Undegassed melt inclusions that fall along plagioclase or clinopyroxene co-crystallization trends are identified in Fig. 4b and c (<6 wt % MgO and <10·5 wt % CaO anhydrous), and are excluded from further modeling. The plag ± cpx-fractionated compositions are screened out to avoid large errors from back-tracking these more complex liquid lines of descent. To compensate for the effects of crystal fractionation on the least fractionated melt compositions, we also adopt the simplifying assumption that olivine is the only liquidus phase. Although there is some scatter in Fig. 4c, these least fractionated, undegassed melt inclusions are consistent with the olivine fractionation trend of increasing CaO with decreasing MgO, in support of this assumption.

The least fractionated melt compositions were back-corrected to primary melts in equilibrium with the mantle by adding equilibrium olivine to each inclusion composition in 0·1% increments, until equilibrium with Fo_{90} [as described by Stolper & Newman (1994) and Kelley *et al.*, (2006)], giving concentrations of elements in the primary magma in equilibrium with mantle olivine (e.g. $TiO_{2(Fo90)}$; see Electronic Appendix 4). On average, this step required addition of ~22% olivine to the melt compositions. To test whether this extent of olivine-only crystallization is appropriate for these magmas, a subset of reconstructed primary melts was used as input to isobaric, forward fractionation models calculated using the Adiabat interface to the MELTS algorithm (Smith & Asimow, 2005). These models show 17–21% crystallization of olivine only for the primary melts from Guguan, Pagan, and Agrigan before saturation with plagioclase or clinoyroxene, consistent with the olivine-addition calculations. To avoid possible artifacts associated with over-correction, any inclusions requiring more than 30% olivine addition ($n = 3$) were also screened out from further modeling. The melt inclusions passing all steps of data filtering for post-entrapment modification, degassing, and fractional crystallization are reported in Table 1 ($n = 20$ from this study; $n = 15$ from Shaw *et al.*, 2008). The complete dataset for all samples is provided in the Electronic Appendix 3.

For direct comparison, similar filtering and correction schemes were applied to pillow glass compositions from the Mariana Trough back-arc basin, following steps modified from Kelley *et al.* (2006). After filtering for degassing, the Mariana Trough dataset (Stolper & Newman, 1994; Gribble *et al.*, 1996, 1998; Newman *et al.*, 2000) was subdivided by H_2O content into three groups: <1·0 wt %, 1·0–1·5 wt %, and >1·5 wt %. These groups also follow parallel liquid lines of descent, with visible offsets related to the delay in plagioclase crystallization caused by increasing magmatic H_2O. The point of plagioclase-in for each group was identified based on inspection of the Mariana Trough data trends in MgO vs Al_2O_3 (see Electronic Appendices 1 and 5). In this case, the Mariana Trough glass dataset is sufficiently large that fractionation trends are clearly defined for all major elements, and these melt

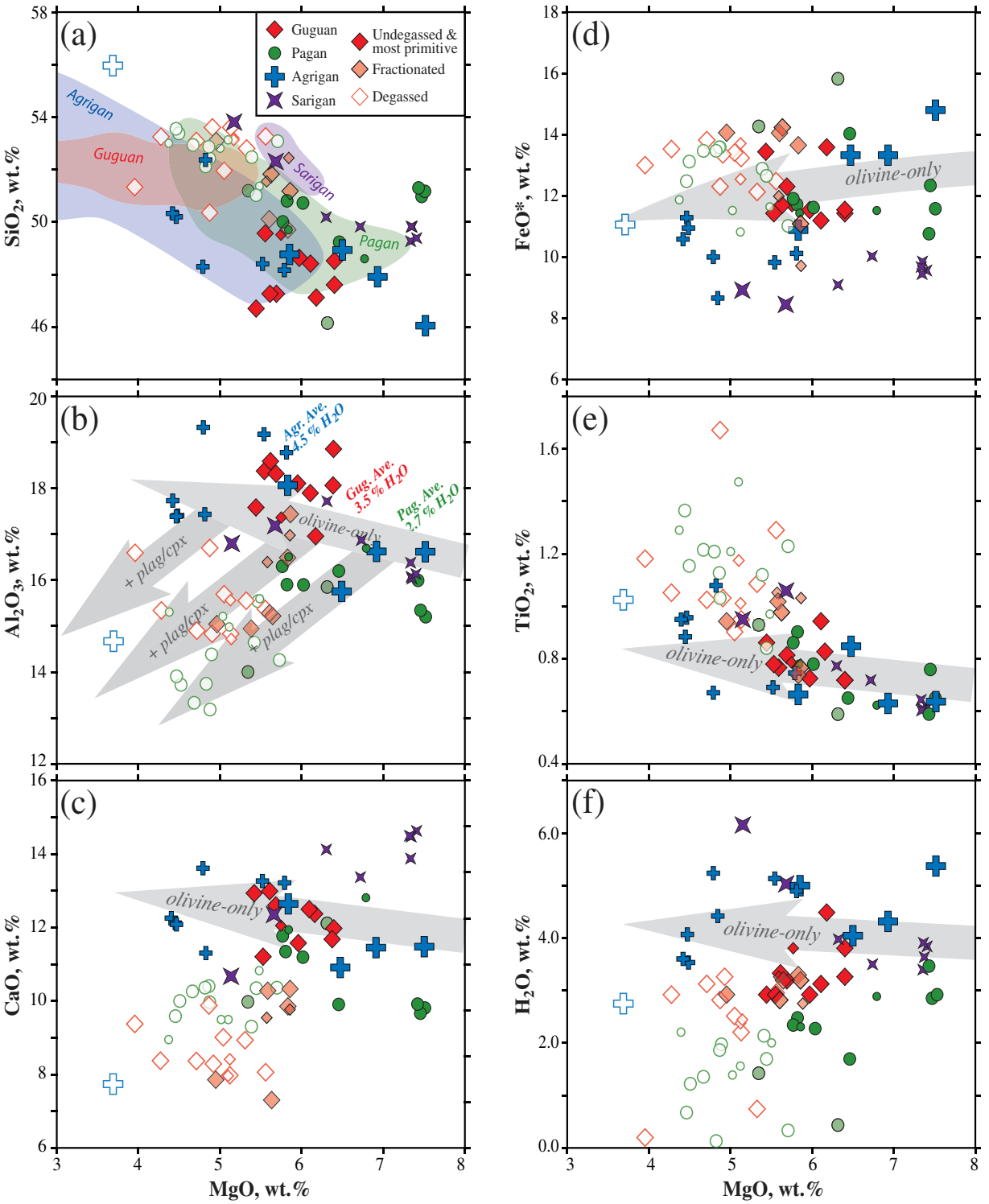

Fig. 4. Plot of major elements vs MgO for Mariana arc olivine-hosted melt inclusions, corrected for post-entrapment olivine crystallization and calculated on an anhydrous basis. The larger symbols are data from this study; smaller symbols are data from Shaw *et al.* (2008). (a) SiO_2 vs MgO. Shaded fields indicate the range of Mariana arc whole-rock lavas for each island (Larson *et al.*, 1974; Dixon & Batiza, 1979; Stern, 1979; Banks *et al.*, 1984; Woodhead, 1989; Elliott *et al.*, 1997). (b) Al_2O_3 vs MgO. (c) CaO vs MgO. (d) FeO* vs MgO, where * indicates total Fe expressed as FeO. (e) TiO_2 vs MgO. (f) H_2O vs MgO, where MgO is expressed on an anhydrous basis, but H_2O is the concentration in the PEC-corrected melt inclusions. The symbol shading scheme in these panels is different from that in other figures. Open symbols indicate probably degassed samples, as identified in Fig. 3 and in the text. Lightly shaded symbols indicate compositions designated as undegassed but identified as fractionated in major element composition, with <6 wt % MgO and <10·5 wt % CaO (anhydrous). Solid symbols identify the least fractionated, undegassed melt inclusion compositions from each island. Average melt H_2O concentrations are calculated from the measured dissolved H_2O contents of the samples represented by the solid symbols (Table 1).

compositions were corrected along average major element vs MgO slopes for these multi-saturated liquid lines of descent to the appropriate point of plagioclase-in, after which each melt was assumed to be saturated with olivine-only (see Electronic Appendices 1 and 5). As with the melt inclusions, these reconstructed primitive melts were traced back to primary mantle melts, assuming 17% $Fe^{+3}/\Sigma Fe$ [average of $Fe^{+3}/\Sigma Fe$ ratios reported for Mariana Trough glasses by Kelley & Cottrell (2009)], by adding equilibrium olivine to each melt in 0·1% increments, until in equilibrium with Fo_{90}. This approach to account for H_2O-based differences in liquid lines of descent (LLDs) differs from that used by Langmuir *et al.* (2006), who used a model to predict LLD offsets for different melt H_2O contents, but then grouped basalts from back-arc basins regionally by spreading segment, rather than strictly by H_2O content, then identified an MgO value at plag-in for each segment. Our approach allows within-segment variations in primary magmatic H_2O, which may produce different LLDs over smaller spatial scales.

RESULTS

The olivine-hosted melt inclusions examined in this study show major element compositions typical of whole-rock basalts from the Mariana arc, although the least-fractionated compositions extend to higher MgO than whole-rock lavas (e.g. Fig. 4a). Although even the most MgO-rich basaltic melt inclusions are not very primitive, this is a characteristic of the Marianas as a whole (e.g. Larson *et al.*, 1974; Dixon & Batiza, 1979; Stern, 1979; Banks *et al.*, 1984; Woodhead, 1989; Elliott *et al.*, 1997). The olivine hosts for the full data suite range in forsterite content from Fo_{69} to Fo_{84}, but the least degassed and least fractionated inclusions are hosted by the most forsteritic olivine from each island ($Fo_{75–84}$). The least degassed inclusions reveal distinct pre-eruptive magmatic H_2O contents characteristic of each island or eruptive unit, and magmatic H_2O generally increases from Pagan (~2·7 wt %) to Guguan (~3·5 wt %) to Agrigan (~4·5 wt %). The two samples from Sarigan indicate distinct magmatic H_2O for each sample [~3·7 wt % for SARI-15 (Shaw *et al.*, 2008); ~5·6 wt % for SA93].

The concentrations of incompatible minor elements (e.g. Na_2O, TiO_2) in basalts are particularly useful for evaluating mantle melting processes in certain systems. At low extents of melting of a homogeneous source, the melt will have relatively high concentrations of incompatible elements, and as the melt fraction (F) increases, their concentrations in the melt decrease progressively as they are diluted. Because of this simple behavior, and the abundance of measurements for these elements in most analyzed igneous rocks, both TiO_2 and Na_2O are widely used to evaluate mantle melting processes beneath mid-ocean ridges (e.g. Klein & Langmuir, 1987; Langmuir *et al.*, 1992; Johnson, 1998). In the Mariana Trough and globally among back-arc basins, increasing $H_2O_{(Fo90)}$ correlates with decreasing $TiO_{2(Fo90)}$ and $Na_2O_{(Fo90)}$ (Fig. 5; Stolper & Newman, 1994; Gribble *et al.*, 1996; Kelley *et al.*, 2006; Langmuir *et al.*, 2006), suggesting a relationship between H_2O input and the extent of mantle melting that has been successfully modeled by several studies (e.g. Stolper & Newman, 1994; Gribble *et al.*, 1996; Wood, 2004; Kelley *et al.*, 2006).

After data filtering and corrections for crystallization, the Mariana arc melts contain higher $H_2O_{(Fo90)}$ (2–5 wt %) than the Mariana Trough basalts (<2 wt %), and the remaining variability among the data is interpreted as diversity in primary magmas at these volcanoes. This interpretation is supported by diversity in the ratios of incompatible minor elements (e.g. K_2O/TiO_2; Na_2O/K_2O) among the melt inclusions, which vary by a factor of two within each sample suite from each volcano. The simple trends from back-arc lavas would predict higher extents of melting and lower concentrations of Na_2O and TiO_2 in Mariana arc melts. Indeed, $TiO_{2(Fo90)}$ decreases with increasing $H_2O_{(Fo90)}$ in the calculated primary arc glass compositions, extending to lower $TiO_{2(Fo90)}$ and higher $H_2O_{(Fo90)}$ relative to the Mariana Trough (Fig. 5a). Moreover, $Na_2O_{(Fo90)}$ also generally decreases with increasing $H_2O_{(Fo90)}$, appearing to extend the trend defined by the Mariana Trough (Fig. 5b), although this trend is more diffuse than that of $TiO_{2(Fo90)}$. Sarigan melts from sample SA93 appear independent of the overall trend of the other Mariana islands in Fig. 5, and their distinct compositions may relate to differences in physical variables beneath this volcano. Overall, the relationships shown in Fig. 5 are consistent with the hypothesis that higher magmatic H_2O contents beneath the arc are connected to higher extents of mantle melting, as long as the mantle source beneath the arc is not extremely depleted relative to the back-arc mantle source.

At subduction zones, however, the mass flux from the dehydrating subducting slab transports not only H_2O but also a veritable cocktail of fluid- and/or melt-mobile elements into the mantle source of arc magmas, potentially complicating the straightforward utilization of these incompatible elements as indicators of arc melting processes. For example, although Na_2O has been identified as a gauge of the overall extent of melting beneath arcs (e.g. Plank & Langmuir, 1988), it is also a primary component of the slab-derived mass flux (e.g. Stolper & Newman, 1994; Kent *et al.*, 2002; Eiler *et al.*, 2005) making it difficult to separate explicitly mantle- vs slab-derived contributions to the Na_2O content of arc melts. In this respect, TiO_2 may be a more sensitive indicator of the extent of melting beneath arcs because, like other 'conservative' high field strength elements (HFSE), TiO_2 has low solubility in low-temperature, rutile-saturated aqueous fluids

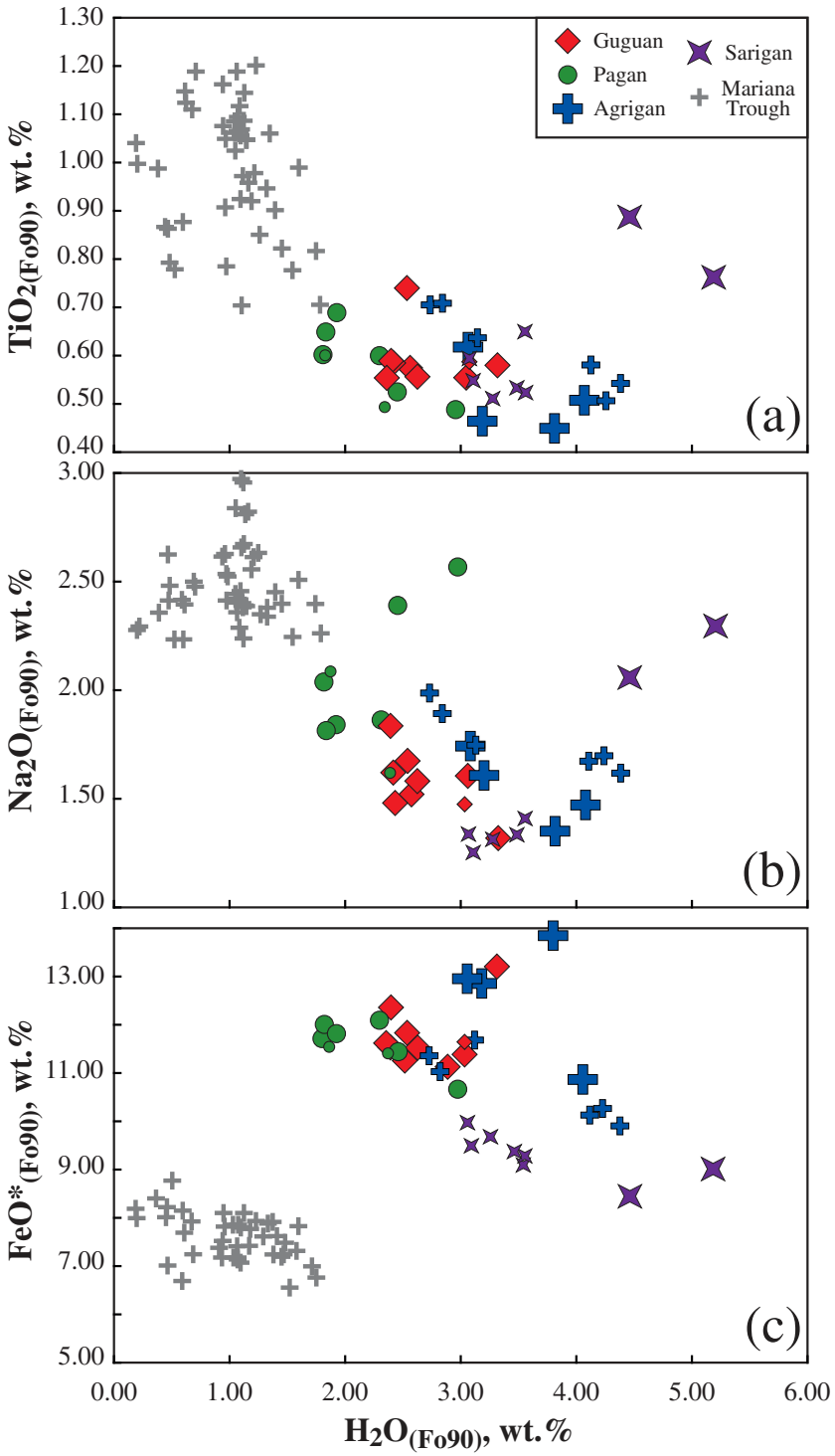

Fig. 5. Major element vs $H_2O_{(Fo90)}$ systematics in calculated primary melt compositions from the Mariana arc and trough, derived from the least degassed and least fractionated melt inclusions identified in Fig. 4. The larger symbols are data from this study; smaller symbols are data from Shaw *et al.* (2008). (a) $H_2O_{(Fo90)}$ vs $TiO_{2(Fo90)}$, (b) $H_2O_{(Fo90)}$ vs $Na_2O_{(Fo90)}$, and (c) $H_2O_{(Fo90)}$ vs $FeO^*_{(Fo90)}$. FeO* is total Fe expressed as FeO.

(Antignano & Manning, 2008) and is less likely to be added in significant quantities to the wedge by the mass flux from the slab (e.g. Stolper & Newman, 1994; Kelley *et al.*, 2006). The characteristic deficiency of HFSE relative to other incompatible trace elements in arc magmas is generally recognized as related to this effect (e.g. Pearce & Parkinson, 1993). Although the TiO_2 flux from the slab is likely to be non-zero, for simplicity, in what follows we assume that TiO_2 is immobile in slab-derived materials, and that its concentration in arc melts is solely a function of the extent of mantle melting and the initial TiO_2 concentration of the mantle source.

Applying the model of Kelley *et al.* (2006), we use the TiO_2 contents of primitive arc magmas to place constraints on the extent of mantle melting and the H_2O concentrations of their mantle sources beneath the Mariana arc. This model uses a simple batch melting relationship to invert melt TiO_2 concentration (i.e. $TiO_{2(Fo90)}$) into the mantle melt fraction (F). The calculated F may then be related to other elements in the melt (e.g. $H_2O_{(Fo90)}$) through the batch melting equation to yield the concentrations of these elements in the mantle source (e.g. $C^o_{H_2O}$). The constraints needed to apply this model are (1) the composition of the primary mantle-derived melt, (2) mantle–melt partition coefficients for TiO_2, H_2O, and any other elements of interest (i.e. D_{TiO2}, D_{H2O}, etc.), and (3) the TiO_2 concentration of the mantle source beneath the Mariana arc (i.e. $C^o_{TiO_2}$). Primary melt compositions were calculated from the most MgO-rich melt inclusions analyzed in this study (see Table 1 and above). The values for D_{H2O} (0·012) and D_{TiO2} (0·04) are those used by Kelley *et al.* (2006). The TiO_2 concentration of the Mariana arc mantle source is the variable to which this model is most sensitive. Plank (2005) used Th/La and Sm/La systematics to show that the Mariana arc taps a mantle source that is more depleted than the source of normal mid-ocean ridge basalt (N-MORB; or the Mariana Trough source, which is similar to N-MORB), and Stolper & Newman (1994) concluded that the Mariana arc mantle source is probably a residue of partial melting beneath the back-arc basin based on significant depletions in HFSE (Ti, Y, Zr) in primitive arc lavas relative to the Mariana Trough. Using whole-rock basalt compositions for Mariana arc lavas from Guguan, Pagan, Agrigan and Sarigan islands (Elliott *et al.*, 1997), we constrain $C^o_{TiO_2}$ beneath the Mariana arc based on systematics in TiO_2/Y ratios as described by Kelley *et al.* (2006). Because all four of the islands included in our study yield similar $C^o_{TiO_2}$ contents based on this analysis (0·104–0·135 wt % TiO_2), we use an average TiO_2 concentration of 0·123 wt % for the mantle source beneath these four islands from the Mariana arc (compared with 0·133 wt % for typical N-MORB sources; e.g. Salters & Stracke, 2004). A complete sensitivity test and Monte Carlo error analysis of this model is presented in Electronic Appendix 1, showing that maximum uncertainties in F are $\pm 0{\cdot}03$ and in $C^o_{H_2O}$ are $\pm 0{\cdot}10$ wt % (absolute), and that most of the model points for each island are statistically separated.

The results of these calculations are shown in Fig. 6a and provide constraints on the extent of melting and the concentration of H_2O in the mantle sources of magmas beneath the Mariana arc, and how these factors may correlate with other physical parameters. Arc melt compositions indicate higher F (~15–25%) than the back-arc basin (≤15%). The concentration of H_2O in Mariana arc mantle sources also reaches >3× higher than in the Mariana Trough (i.e. >0·9 wt % H_2O for the Agrigan sources, vs a maximum of 0·3 wt % for the calculated Mariana Trough sources). Such high mantle H_2O concentrations clearly exceed the storage capacity of H_2O in nominally anhydrous mantle minerals (e.g. Hirschmann *et al.*, 2005), but would be permissible if a hydrous phase is stable in the mantle wedge (e.g. chlorite; Grove *et al.*, 2006) or if sub-arc melting is a fractional process driven by incremental water addition (e.g. Kelley *et al.*, 2006).

The results of this modeling reveal a positive relationship between melt fraction and the water content of the mantle beneath these Mariana arc volcanoes (Fig. 6). Similar positive relationships are defined both for each volcano, and for the group of four volcanoes taken together (excluding glass inclusions from Sarigan sample SA93). Although distinct from the others, the Sarigan SA93 sample also indicates a positive relationship between $C^o_{H_2O}$ and F. Previous studies have proposed linear (e.g. Stolper & Newman, 1994; Kelley *et al.*, 2006) and non-linear (e.g. Katz *et al.*, 2003; Langmuir *et al.*, 2006; Portnyagin *et al.*, 2007) shapes to the melting function relating mantle H_2O content and F, although the data range revealed here neither constrains the functional shape well nor supports a significantly non-linear shape. Although the Mariana arc melts indicate higher mantle H_2O concentrations and higher extents of melting than the back-arc, the slopes are different and the arc is unlikely to be a simple extension (whether curved or linear) of the back-arc trend. Collectively and for single islands, the arc melts indicate a steeper slope (i.e. smaller ΔF for a given increase in mantle H_2O content) than the back-arc. We note, however, that consideration of a range of values for D_{TiO2} and $C^o_{TiO_2}$ strongly influences the value of the apparent F-axis intercept (i.e. melt fraction at $C^o_{H_2O} = 0$) of the arc trends. Either a much higher value of D_{TiO2} (~0·16) or a much more depleted mantle source ($C^o_{TiO_2} = \sim 0{\cdot}06$) will result in a zero F intercept for the arc. Changes in these variables do not, however, have a significant influence on the slope of the arc or trough trends, and we thus emphasize that no value for either D_{TiO2} or $C^o_{TiO_2}$ will cause the arc to lie on a simple linear extension of the Mariana Trough trend.

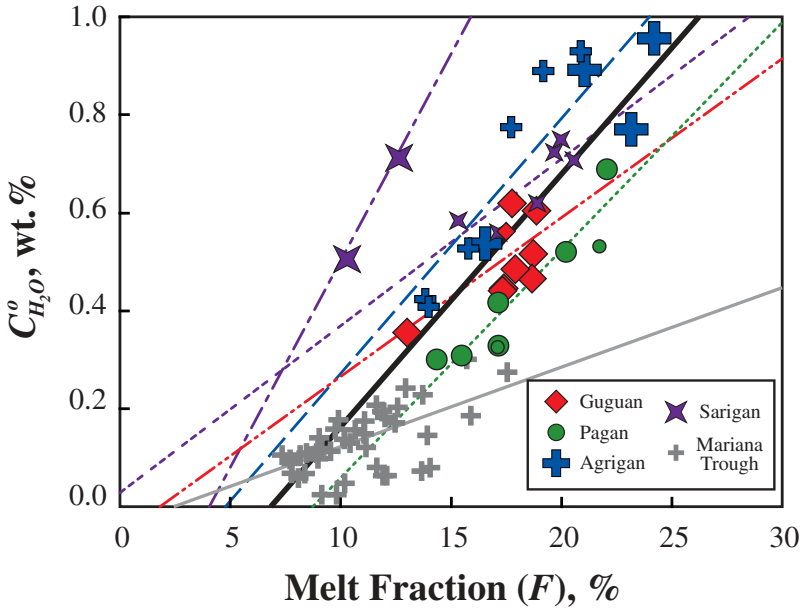

Fig. 6. Plot of $C^o_{H_2O}$ (i.e. H_2O concentration in the mantle source; see text) vs melt fraction (F) for Mariana arc and trough modeled data. The lines shown are least-squares linear regressions through the data for each island, the whole arc (excluding SA93) and the back-arc basin. The continuous gray line is the Mariana Trough ($y = 1{\cdot}63 \times -0{\cdot}05$; $r^2 = 0{\cdot}40$), the dotted line is Pagan island ($y = 5{\cdot}10 \times -0{\cdot}41$; $r^2 = 0{\cdot}87$), the dash–double-dot line is Guguan island ($y = 3{\cdot}21 \times -0{\cdot}06$; $r^2 = 0{\cdot}43$), the long-dashed line is Agrigan island ($y = 5{\cdot}20 \times -0{\cdot}26$; $r^2 = 0{\cdot}78$), the dash–dot line is Sarigan island sample SA93 from this study ($y = 8{\cdot}62 \times -0{\cdot}38$; $r^2 = 1$), the triple-dot line is Sarigan island data from Shaw *et al.* (2008) ($y = 3{\cdot}36 \times +0{\cdot}03$; $r^2 = 0{\cdot}71$), and the bold black line is all of the Mariana arc data, excluding SA93 samples ($y = 5{\cdot}10 \times -0{\cdot}35$; $r^2 = 0{\cdot}55$).

DISCUSSION

Interpretation of the data with respect to melting processes taking place beneath the Mariana arc requires constraints on the physical state of the mantle wedge. In the following discussion, the arc and back-arc basin trends in the Mariana system are examined together, in the light of variables likely to play important roles in the mantle melting process. When viewed together, the arc and back-arc data support the interpretation of TiO_2 vs H_2O trends as melting relationships, rather than mixing of end-member melts, which is further reinforced by seismic tomography models of the Mariana system. We show that the arc melt inclusion data ultimately reflect a combination of three key variables: the geotherm, the fertility of the mantle wedge (a function of source depletion), and the amount of H_2O added to the mantle wedge. We develop a model that incorporates these variables and successfully reproduces melting trends shown by the Mariana data.

Mixing vs melting

The modeled trends in $C^o_{H_2O}$ vs F for the Mariana arc and trough shown in Fig. 6 suggest a direct link between the magnitude of H_2O addition to the mantle wedge and the extent of mantle melting. From one perspective, each melt inclusion or glass records a melt fraction driven by a certain amount of water addition to the mantle wedge (Kelley *et al.*, 2006). Alternatively, the trends in H_2O vs TiO_2, or $C^o_{H_2O}$ vs F, for back-arc basin basalts could result from mixing of melts produced by two separate end-member processes: (1) nominally anhydrous, pooled, fractional melting analogous to the melting processes beneath normal mid-ocean ridges, giving rise to a low-F, low-H_2O, high-FeO* (i.e. FeO* is total Fe expressed as FeO), high-TiO_2 final melt, and (2) low-pressure, hydrous, equilibrium melting that produces a high-degree melt with high H_2O, low FeO*, and low TiO_2 (Langmuir *et al.*, 2006). In a physical sense, these two distinct melts could originate from the arc-distal, 'dry' side of a triangular ridge-like melting regime, and a shallower, water-rich melting regime on the arc side of the mantle wedge, and the compositional trends of back-arc basin basalts could be explained through variable, shallow mixing of magmas from these two separate melting systems.

These new melt inclusion data for the Mariana arc have particular bearing on the question of mixing vs melting relationships reflected in melt compositions across the Mariana arc–back-arc system. If the compositions of Mariana Trough basalts reflect mixing of MORB- and arc-like end-members, we would expect the Mariana arc to define a linear extension of the Mariana Trough data array, particularly in terms of H_2O, TiO_2, and FeO*, and possibly to exemplify the shallow, 'arc-like' H_2O-rich, end-member melt. Although the arc data certainly extend the back-arc trend in H_2O vs TiO_2 (Fig. 5a), the transitions between the arc and back-arc basin basalts are nonlinear for these elements. Moreover, the difference between arc

and back-arc basin melts in the Mariana system is clearly apparent in H_2O vs FeO* (Fig. 5c). Total FeO* concentrations of water-rich Mariana arc melts are highly enriched (>2× in some cases) relative to hydrous melts from the Mariana Trough, and simple linear mixing between arc and back-arc magmas cannot explain the data array in Fig. 5c. If the FeO* concentrations of the primary arc magmas contain a much greater fraction of Fe_2O_3 than do back-arc magmas (i.e. arc magmas are significantly more oxidized than back-arc magmas), then the absolute FeO concentrations of magmas from the two settings may be more similar than the FeO* content indicates on its own, but in this case the Fe_2O_3 variations would then not be explained through mixing. Furthermore, examination of the trace element and isotopic systematics of the Mariana arc and trough exclude simple mixing of arc components into the back-arc (e.g. Stolper & Newman, 1994; Gribble *et al.*, 1996; Pearce *et al.*, 2005). The observed geochemical trends among the arc and back-arc data are thus interpreted as melting relationships.

Separate arc and back-arc basin melting regimes

Conventionally, arc and back-arc basin melting regimes are often envisioned and modeled as physically separate. Prevailing models of magma generation for arcs vs back-arc basins invoke compositionally distinct mantle sources for each, with back-arcs sampling mantle that is broadly similar to the range of MORB sources (e.g. Stolper & Newman, 1994; Kelley *et al.*, 2006; Langmuir *et al.*, 2006) and associated arcs tapping mantle that is relatively more depleted in incompatible HFSE (e.g. Woodhead *et al.*, 1993; Pearce *et al.*, 2005). Mantle flow vectors and magma geochemistry suggest that mantle upwelling beneath back-arc spreading centers leads to an episode of melt extraction that 'preconditions' the mantle (e.g. Woodhead *et al.*, 1993; Pearce, 2005; Pearce *et al.*, 2005) before it then moves horizontally toward the wedge corner and melts a second time beneath the arc (e.g. Hawkins *et al.*, 1990; Stolper & Newman, 1994; Kincaid & Hall, 2003). Despite broad similarities to mid-ocean ridges in terms of overall structure (e.g. Tamaki, 1985; Taylor & Martinez, 2003), mantle temperature (Klein & Langmuir, 1987; Kelley *et al.*, 2006; Langmuir *et al.*, 2006; Wiens *et al.*, 2010), and the presence of relatively anhydrous MORB-type lavas, back-arc basin basalts (BABB) are geochemically distinct from MORB in many ways, including elevated H_2O, large ion lithophile elements, and light rare earth elements, suggestive of an 'arc-like' component infiltrating the back-arc mantle source (e.g. Fryer *et al.*, 1981). However, new seismic attenuation results for the Mariana mantle wedge (Pozgay *et al.*, 2009), in addition to geochemical relationships in the Marianas (see above), generally support the view that the mantle sources of arc and back-arc magmas are physically separated from one another, particularly at shallow depths (Fig. 7).

Langmuir *et al.* (2006) show a correlation of increasing $H_{(8\cdot0)}$ with decreasing $Fe_{(8\cdot0)}$ (i.e. H_2O and FeO* traced along a liquid line of descent to the concentrations equivalent at 8·0 wt % MgO) in the Mariana Trough, arguing that H_2O-rich melts originate at shallower depths than anhydrous melts. $Fe_{(8\cdot0)}$ is a powerful indicator of melting pressure in mid-ocean ridge systems, where variations in primary MORB melt chemistry can be directly compared by choosing a single reference point along comparable LLDs (Klein & Langmuir, 1987). Adapting this approach for back-arc basin basalts, however, requires accurate constraints on the variations of the liquid line of descent caused by variations in H_2O content (see above), and the selection of an appropriate reference point along the LLD. At 8·0 wt % MgO, most dry basalts are not directly comparable with hydrous basalts because of differences in the LLDs. Dry basalts would thus be under-corrected for crystal fractionation, yielding, for example, too high $Fe_{(8\cdot0)}$ relative to wetter basalts that originated from a parent magma with the same FeO*. In the present study, we choose MgO = 8·5 wt % as the point of plagioclase-in for Mariana Trough basalts with <1·0 wt % H_2O (see above), which is consistent with MORB systematics (Kelley *et al.*, 2006), and then correct all compositions back to primary melts in equilibrium with Fo_{90} for direct comparison. These methods result in a weak correlation between FeO* and H_2O in Mariana Trough basalts (Fig. 5c) that could relate less to mean pressures of melting than to the expansion of the olivine liquidus volume and coincident decrease in normative olivine in the melt with increasing H_2O and decreasing T (e.g. Kushiro, 1972; Stolper & Newman, 1994). The interpretation of co-variations in $H_{(8\cdot0)}$–$Fe_{(8\cdot0)}$ is thus ambiguous, and in a subsequent section we directly assess the relationship between melt composition and quantitative estimates of P–T conditions of melt equilibration.

Modes and conditions of melting beneath the Mariana arc

Wet melt productivity

Taken as a whole, the Mariana arc melt compositions indicate a positive correlation between water content in the magmas (and their sources) and proxies for melt fraction (e.g. TiO_2; Fig. 5). The slope of each trend in Fig. 6, expressed as $dF/dC^o_{H_2O}$, is one indication of the productivity of water-fluxed melting. Differences in slope are unlikely to be the result of differences in model variables, such as $C^o_{TiO_2}$ or D_{TiO2}, because the mantle source is not expected to vary significantly between these volcanoes (Plank, 2005; and see above), and changes in these parameters have only a minor influence on the slope (Kelley *et al.*, 2006, and see Electronic Appendix 1). Instead, if the

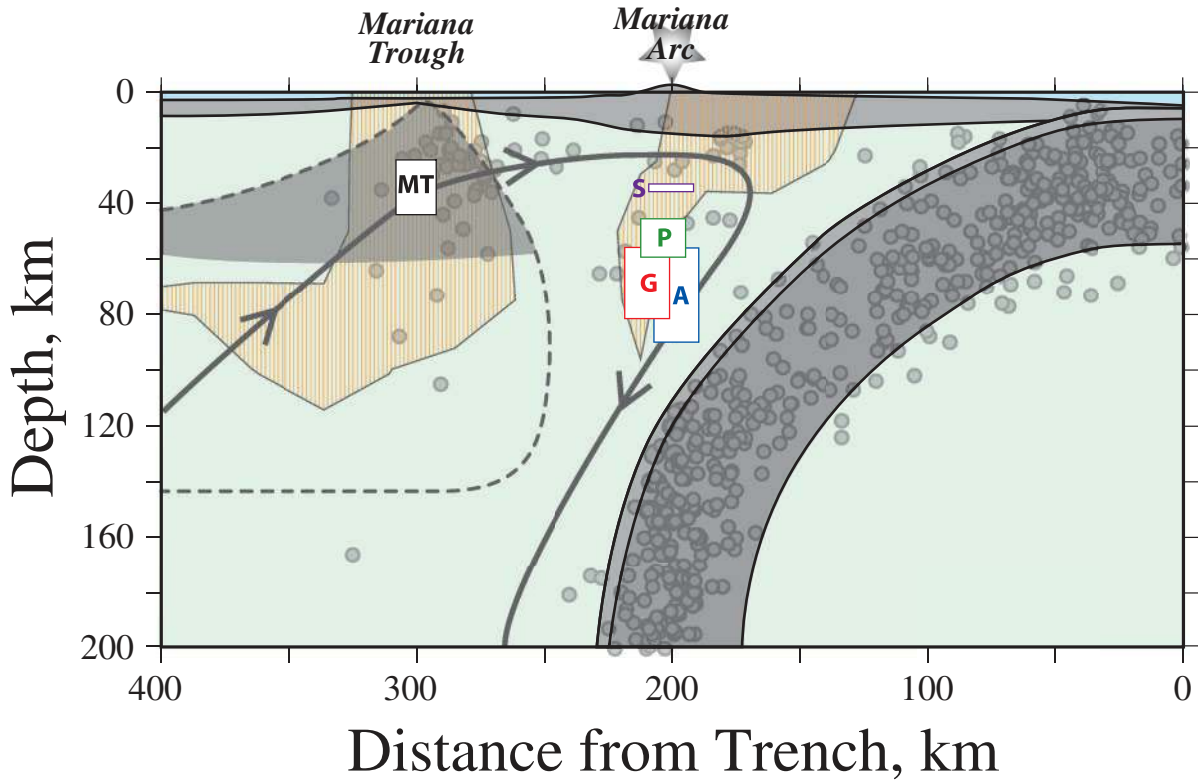

Fig. 7. Scaled schematic illustration showing a cross-section of the Mariana subduction zone, with the locations of melt equilibration within the mantle wedge for the Mariana arc and trough, as constrained by thermobarometry. The small, shaded circles are earthquake data from England *et al.* (2004), and the crustal thickness is taken from the seismic velocity model of Takahashi *et al.* (2007). The trace of the subducting plate is drawn to encompass the majority of the seismicity, and the asymmetric triangle beneath the Mariana Trough represents the anhydrous melting regime for the back-arc spreading center where vertical mantle upwelling is deflected towards the slab, guided by the numerical models of Conder *et al.* (2002), for a mantle T_p of 1350°C. The dashed line outlines the approximate melting triangle that would apply for H_2O-saturated mantle melting beneath the Mariana Trough. The gray line with arrows traces an approximate vector of solid flow through the mantle wedge. The vertically striped fields are regions of high seismic-wave attenuation in the mantle wedge ($1000/Q_p \geq 12$; Pozgay *et al.*, 2009). White boxes indicate the depth ranges of melt equilibration for the Mariana arc islands and the Mariana Trough; horizontal offsets of the arc boxes are not significant and the boxes are shown in this way only to distinguish the range for each island. A, Agrigan; G, Guguan; P, Pagan; S, Sarigan; MT, Mariana Trough.

mantle composition and the magnitude of the water flux are similar, then differences in wet melt productivity may be governed by physical conditions in the mantle wedge. For example, Kelley *et al.* (2006) showed an empirical correlation between $dF/dC^o_{H_2O}$ and mantle potential temperature (T_p) among back-arc basin basalts. Following these systematics, the arc slopes could be interpreted as reflecting overall lower mantle temperatures under the arc than under the back-arc. Although this interpretation is consistent within back-arc basin data arrays, the arc data require the additional consideration of melting pressure and mantle fertility, for which we develop new models here (see below). The key parameter in recent hydrous melting models is the temperature (T) relative to the dry solidus (T_o). Comparisons of parameterizations of hydrous melting (Langmuir *et al.*, 2006; Portnyagin *et al.*, 2007) with the modeled arc data require temperatures near or below the dry peridotite solidi specific to these models (e.g. Fig. 8a; curves for $T - T_o = 0$ to -25). The arc melting trends require melting to occur largely below the dry solidus (i.e. $T - T_o < 0$) and the back-arc melting to occur above the dry solidus (i.e. $T - T_o > 0$). This appears to be a general feature of arcs vs back-arc basins, based on the data presented here and shown by recent studies (e.g. Langmuir *et al.*, 2006; Portnyagin *et al.*, 2007).

Parameterizing hydrous melting

Previous hydrous melting models are largely isothermal and isobaric, or consider melting over a limited range of pressure and mantle composition (Gaetani & Grove, 1998; Hirschmann *et al.*, 1999; Katz *et al.*, 2003; Langmuir *et al.*, 2006). Here, we consider the specific effects of pressure and mantle fertility on wet melting productivity. Langmuir *et al.* (2006) developed a re-formulation of the

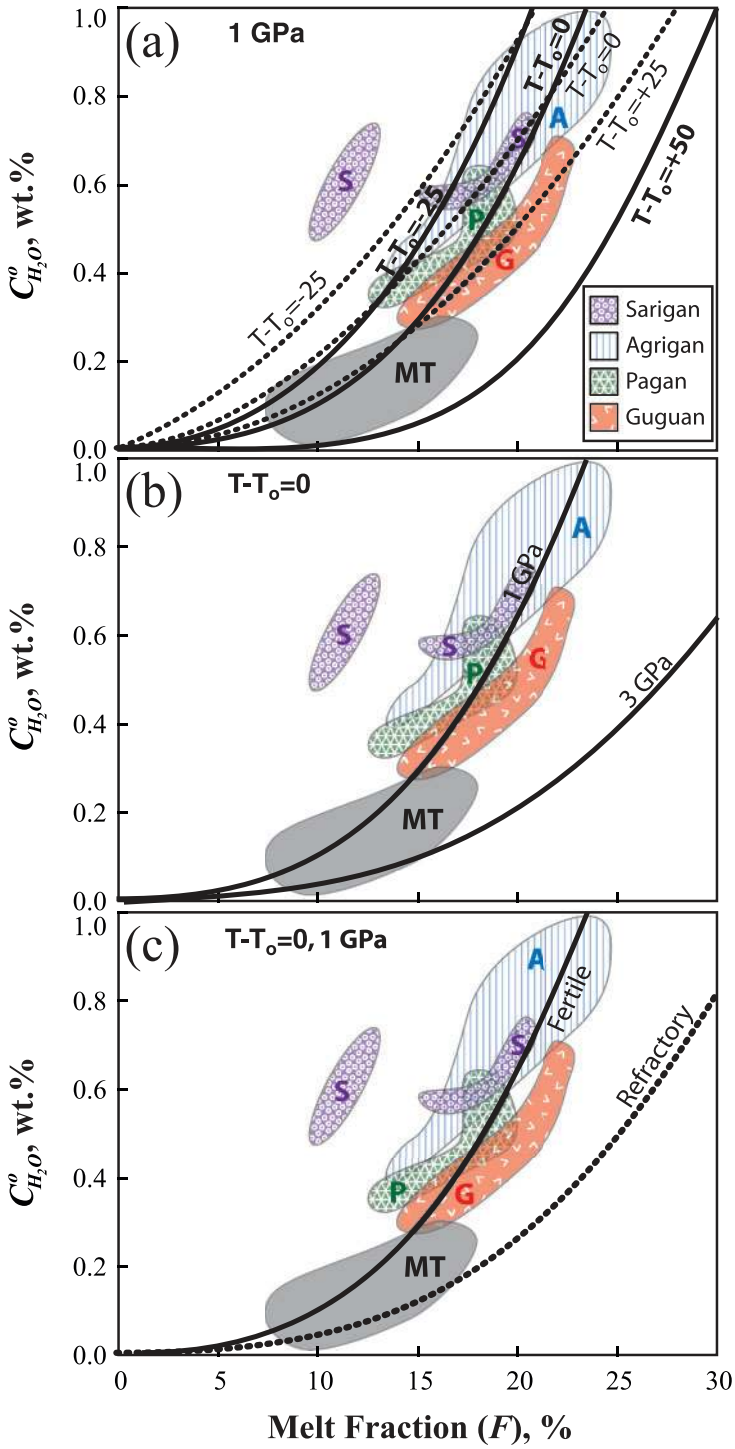

Fig. 8. Plots of $C^o_{H_2O}$ vs melt fraction (F) showing melting curves derived from various models. (a) Wet melting models from previous studies, showing the effect of changing temperature at constant pressure and mantle composition. The continuous lines are the model of Langmuir *et al.* (2006) for a range of temperatures relative to the solidus ($T - T_o$) at 1 GPa. The dotted lines are the model curves of Portnyagin *et al.* (2007), which use the parameterization of Katz *et al.* (2003). (b) Wet melting model curves derived from equation (4), for fertile peridotite melting at the dry solidus (i.e. $T - T_o = 0$) over a 1–3 GPa range of pressure. The curvature of the model trend changes significantly as pressure increases. (c) Wet melting model curves derived from equation (4) for fertile and refractory peridotite models, at the temperature of the solidus (i.e. $T - T_o = 0$) for each case at 1 GPa.

melting parameterization of Katz *et al.* (2003), using the linear expression of F vs T for a set of 1 GPa, anhydrous peridotite melting experiments (Baker & Stolper, 1994; Baker *et al.*, 1995; Hirschmann *et al.*, 1998) to parameterize F as a function of $C^{o}_{H_2O}$ and T at 1 GPa. One form of their equation is

$$C^{o}_{H_2O} = [D_{H_2O}(1-F)+F]\left[\frac{T-1235-539F}{-60}\right]^{1.85} \quad (1)$$

where 1235 is the temperature in °C of the dry solidus (i.e. T_o) at 1 GPa and 539 is $[\partial T/\partial F]_P$ (i.e. ~5°C/%) at 1 GPa, derived from the anhydrous experiments (see fig. 33 of Langmuir *et al.*, 2006). Melting functions calculated using this model are isothermal and isobaric, applying to a specific solidus only at 1 GPa, and the approximate slope (i.e. $dF/dC^{o}_{H_2O}$) of the melting curve does not change significantly with changing T relative to the dry solidus at this pressure (Fig. 8a). Combining this analysis with the 3–7 GPa anhydrous peridotite melting experiments of Walter (1998), however, reveals a significant pressure dependence to $[\partial T/\partial F]_P$ (Fig. 9a), which decreases with increasing P. This effect will lead to greater wet melting productivity at higher pressure, and can be incorporated into equation (1) in the following way. We use Walter's experiments to fit a simple expression for the pressure dependence of $[\partial T/\partial F]_P$ for fertile peridotite (Fig. 9b):

$$\left[\frac{\partial T}{\partial F}\right]_P = x\ln(P)+y \quad (2)$$

where the coefficients $x=-221{\cdot}34$ and $y=536{\cdot}86$ and P is pressure in GPa. We also adopt the recommended solidus for upper mantle peridotite from Hirschmann (2000) (Fig. 7c):

$$T_o = aP^2+bP+c \quad (3)$$

where T_o is the temperature of the dry solidus in °C, P is pressure in GPa, and coefficients are $a=-5{\cdot}1404654$, $b=132{\cdot}899012$, and $c=1120{\cdot}66061$. Hereafter, models using the coefficients provided here are referred to as the 'fertile' peridotite case. Substituting these terms into equation (1) gives the following:

$$C^{o}_{H_2O} = [D_{H_2O}(1-F)+F] \times \left[\frac{T-(aP^2+bP+c)-(x\ln(P)+y)F}{-60}\right]^{1.85} \quad (4)$$

Equation (4) is similar to the formulation of Langmuir *et al.* (2006) at 1 GPa, but allows pressure to be varied and thus provides a simple parameterization of hydrous melting that can be applied at different temperatures and pressures. Figure 8b shows the change in shape of this wet melting function along the dry solidus (i.e. $T-T_o=0$) from 1 to 3 GPa, confirming that increasing pressure results in a coincident increase in wet melt productivity. Such an effect may contribute to the observed increase in wet melting productivity with increasing mantle T_p beneath back-arcs globally (Kelley *et al.*, 2006; Langmuir *et al.*, 2006), because mantle of higher T_p will melt at higher mean pressures than mantle of lower T_p (Langmuir *et al.*, 1992). Figure 8b also predicts that wet melts may equilibrate at higher mean pressures beneath the Mariana Trough than the Mariana arc, given that the trough indicates a greater wet melt productivity than the arc (Fig. 6), although we will demonstrate below that the opposite is true when appropriate pressures, temperatures, and mantle fertility are considered together.

Mantle fertility is an important effect to include in the wet melting parameterization because refractory mantle (i.e. mantle from which melt has previously been removed) will melt at higher solidus temperatures and higher melt productivities than fertile mantle for a given pressure and water content (Asimow *et al.*, 1997; Wasylenki *et al.*, 2003). Many studies also provide constraints on the solidus of nominally anhydrous upper mantle, which may vary considerably with several compositionally dependent variables including alkali content (e.g. Hirschmann *et al.*, 1998; Hirschmann, 2000) and prior melt depletion (e.g. Wasylenki *et al.*, 2003). Substituting different dry solidus equations and melt productivities [i.e. alternative coefficients from equations (2) and (3)] into equation (4) produces appropriate melting functions relevant to the specified mantle. Here, we use constraints from melting experiments on composition DMM1, intended to represent an upper mantle peridotite from which some melt has been removed (Wasylenki *et al.*, 2003), to parameterize melting of a more refractory mantle composition. The solidus of DMM1 is constrained at 39°C higher than the recommended solidus of Hirschmann (2000) at 1 GPa [giving a new value for the coefficient $c=1159{\cdot}66061$ for equations (3) and (4)] and DMM1 anhydrous melt productivity in the lherzolite field at 1 GPa is somewhat higher than the productivity of the more fertile MM3 peridotite (Fig. 9a and c; Wasylenki *et al.*, 2003). We model the change in DMM1 melt productivity with pressure as proportional to the fertile case, giving coefficients for equations (2) and (4) of $x=-136{\cdot}88$ and $y=332{\cdot}01$. Models using the coefficients provided here are hereafter referred to as the 'refractory' peridotite case. It is important to emphasize that both the fertile and refractory cases developed here are appropriate for lherzolite melting. The DMM1 composition exhausts cpx in the residue at $F\sim 0{\cdot}1$, at which point melt productivity decreases, reflecting less productive melting with a harzburgite residue (Wasylenki *et al.*, 2003); the model developed here does not account for this additional complexity because our primary goal is to characterize first-order differences between melting lherzolite of contrasting fertility.

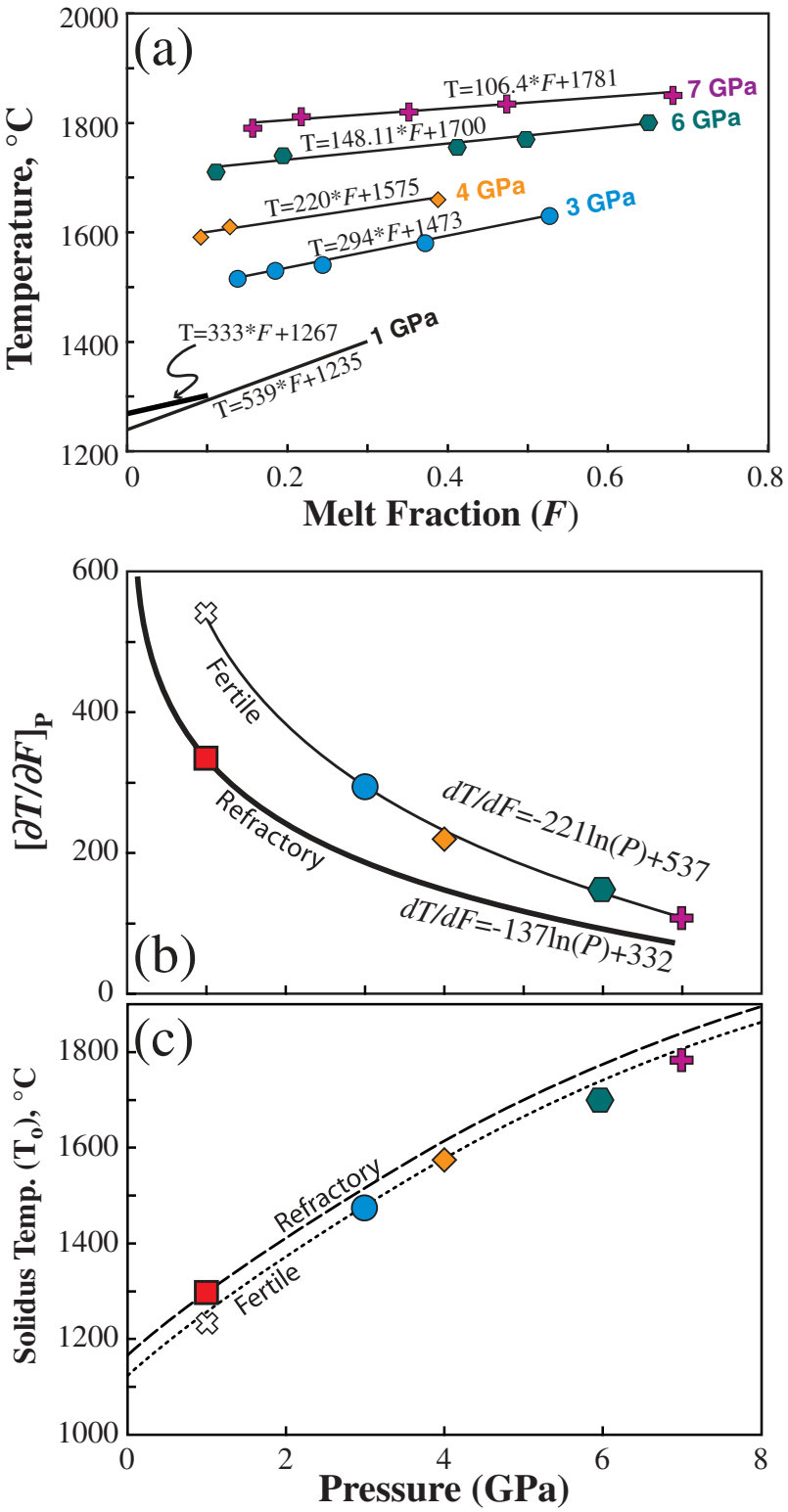

Fig. 9. Experimental constraints on melting parameters across a range of pressures. (a) Plot of temperature vs melt fraction for the 1 GPa partial melting experiments cited by Langmuir *et al.* (2006; fine line labeled 1 GPa), and for the 3–7 GPa experiments of Walter (1998). Symbols show these experimental data at 3 GPa (circles), 4 GPa (diamonds), 6 GPa (hexagons), and 7 GPa (crosses). Linear regressions through the datasets at each pressure, as written on the figure, provide constraints on $[\partial T/\partial F]_P$ as a function of pressure. The bold line is the 1 GPa depleted lherzolite trend of Wasylenki *et al.* (2003). (b) Plot of $[\partial T/\partial F]_P$ vs pressure for the experiments shown in (a). The fertile 1 GPa suite is shown as the 'x' symbol, the depleted 1 GPa suite is shown as the square symbol. The fine curve is a least-squares regression through the data (equation on the figure), which provides the coefficients for the fertile case of equation (2) in the text. The bold curve is proportional to the fertile case, constrained to pass through the square symbol, and provides coefficients for the refractory model. (c) Plot of solidus temperature (T_o) vs pressure (i.e. P–T curves of the mantle solidus) for the experiments in (a) and (b). The recommended fertile solidus of Hirschmann (2000; dotted line) and the depleted mantle solidus of Wasylenki *et al.* (2003; dashed line) are shown.

The effect of melting fertile vs refractory lherzolite at a given P and T is illustrated in Fig. 7c for the two mantle compositions described above. These specific choices of peridotite composition are intended to provide examples of well-constrained mantle materials and phase relations that reflect variations in natural systems that arise from prior melt extraction. We do not develop here a model for how melt extraction quantitatively affects the solidus or productivity of the residual peridotite; rather we use these established examples to infer the first-order effects. The impact of the choice of peridotite on the melting function is clear in Fig. 8c, where the refractory case gives a much higher melt productivity relative to the fertile case. At first glance, this result predicts that melting refractory mantle beneath the arc should project to much higher extents of melting than those indicated by the melt inclusion data, but the effect of mantle fertility has not yet been integrated with the effects of temperature and pressure of melting. In the following sections, we will constrain relevant temperatures and pressures of melt equilibration beneath the Mariana arc and trough, and assess the competing effects of pressure, temperature, and mantle fertility on melting beneath the Mariana system.

Thermobarometry

Thermobarometric information, as recorded by melt compositions and mineral–melt equilibria, provides a means to quantify the pressures and temperatures of equilibration of primary melts in the mantle wedge. To calculate P–T conditions recorded by primary Mariana arc and back-arc melts, we use the recent model of Lee *et al.* (2009), which quantifies in a thermobarometer the well-known effects of pressure on the SiO_2 content and temperature on the MgO content of olivine + orthopyroxene-saturated mantle melts. These P–T constraints, however, are not necessarily straightforward to interpret. They may represent the final conditions of equilibration of a single batch melt, or a continuously interacting melt that percolates upward through the solid mantle and reacts constantly along its path, in which case these conditions are very different from the potential temperature of the mantle; in general they are substantially cooler than T_p as a result of cooling from the heat of fusion. The P–T constraints could alternatively represent some intermediate P–T conditions along a melting path. In this case, P–T would be similar to the mean P and T of polybaric, fractional, pooled melts, although not an exact mean because the pooled melt is a mixture that would not invert back to any single point or mean.

The results of thermobarometry calculations for the Mariana Trough indicate pressures of equilibration of 0·6–1·2 GPa (±0·2 GPa), which are consistent in range with the polynomial SiO_2 barometer of Wang *et al.* (2002), but are systematically lower by ~0·4 GPa. The P–T conditions of the drier Mariana Trough melts lie along a melting path for mantle with a potential temperature of ~1350°C (Fig. 10a), identical to that estimated by Langmuir *et al.* (2006) and Wiens *et al.* (2006). In this case, the calculated absolute P and T are similar to the mean values along the melting path, consistent with pooling of polybaric melts, as for mid-ocean ridge basalts (Langmuir *et al.*, 1992). On the other hand, the wet Mariana Trough melts record substantially cooler absolute T (~1250 ± ~40°C) at similar P (~1 GPa), also nearly identical to that estimated by Langmuir *et al.* (2006) for their wet melt end-member, using a completely independent method. Despite some ambiguities in interpretation, the thermobarometer of Lee *et al.* (2009) returns intermediate P and T for the Mariana Trough, similar to those derived from other methods, consistent with polybaric pooling of melts along the melting path.

In contrast, the Mariana arc melts yield a larger pressure range, extending to much higher values than the Mariana Trough (1·0–2·4 ± 0·2 GPa), as well as higher overall temperatures spanning a much broader range (~1200–1400 ± ~40°C; Table 2; Fig. 10). The contrast in P–T conditions between the Mariana arc and trough indicates hotter, deeper melting beneath the arc than the back-arc. These results are suggestive of the different physical processes of melting and melt aggregation in these two settings. Beneath the Mariana Trough, H_2O-fluxed melting could begin at great depth, where slab-derived H_2O is introduced into the mantle wedge, but all melts from the Mariana Trough record P–T conditions at shallow depths, within the predicted pressure range of the anhydrous melting triangle (Fig. 7). Moreover, there is no strong correlation between pressure of equilibration and the H_2O content of the mantle in the Mariana Trough (Fig. 10b). These observations suggest that wet melts passing through the anhydrous back-arc melting triangle equilibrate there at shallow depth, recording P–T conditions of mean or later stages of melting and retaining no record of their depth of origin in their major element composition.

If the ambient mantle T_p beneath the Mariana Trough is ~1350°C (Langmuir *et al.*, 2006; Wiens *et al.*, 2006), then the base of the dominant (dry) melting triangle is ~2·0 GPa (Figs 7 and 10). A melting triangle extending from 2·0 to 0·2 GPa will generate melts with mean pressures of between 0·7 and 1·3 GPa, for equilibrium and fractional melting, respectively (Langmuir *et al.*, 1992; see their fig. 50). This is very similar to the range observed (Fig. 10), and suggests that the back-arc melts are dominated by the melting systematics driven by the upwelling mantle beneath the spreading center, much as at mid-ocean ridges. Absolute mantle temperatures colder than the mantle potential temperature of 1350°C are consistent with cooling effects during adiabatic melting, where temperature decreases during melting so as to

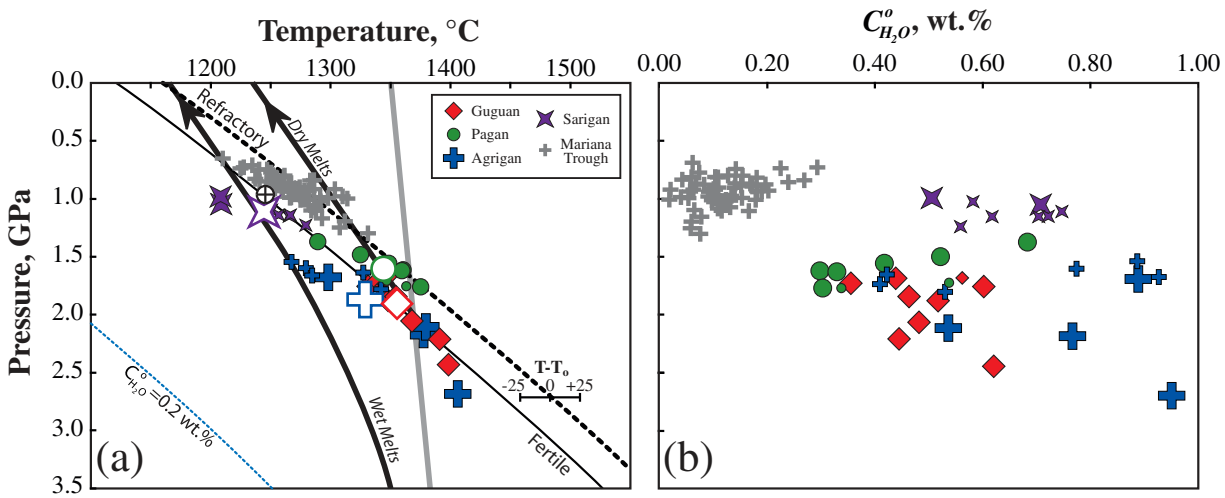

Fig. 10. Plot of melt equilibration pressure vs equilibration temperature and $C^o_{H_2O}$, determined using the thermobarometer of Lee *et al.* (2009). (a) Equilibration pressure vs temperature for Mariana arc and trough melts. Filled symbols are constraints from single glasses; large open symbols are averages of the glass results from each island (Table 2). The fine continuous curve is the recommended fertile anhydrous solidus of Hirschmann (2000), and the dashed curve is the depleted mantle (refractory) solidus of Wasylenki *et al.* (2003). The thick, continuous gray line is an adiabatic ascent path for $T_p = 1350°C$. A T_p of 1350°C is assumed for the Mariana Trough. The thick, continuous black line with arrow, labeled 'Dry Melts,' is the adiabatic melting path for $T_p = 1350°C$ above the solidus of Hirschmann (2000). The analogous curve labeled 'Wet Melts,' is a schematic melting path for $T_p = 1350°C$ above a hydrated solidus with 0·2 wt % H_2O (fine dotted line). The crossed circle at 1240°C and 1 GPa represents the P–T conditions of the wet Mariana Trough melt end-member of Langmuir *et al.* (2006). The scale bar in the lower right of the panel illustrates the variable $T - T_o$, where negative values indicate that the temperature is below the reference solidus at a given pressure, and positive values indicate temperatures above the reference solidus at a given pressure. Consistent with the melt productivity model in Fig. 11, the Mariana Trough melts record conditions above the more fertile, anhydrous solidus, whereas the Mariana arc melts record conditions below the more refractory anhydrous mantle solidus. (b) Equilibration pressure vs $C^o_{H_2O}$. Both the Mariana arc and trough show no correlation between equilibration pressure and water content.

supply the heat of fusion. The Mariana Trough P–T range in Fig. 10a probably reflects cooling from melting mantle of $T_p = 1350°C$ that intersects either the anhydrous solidus, melting to a lower extent and cooling less ('dry melts' curve in Fig. 10a), or a hydrated solidus at higher pressure, melting to a greater extent and cooling more ('wet melts' curve in Fig. 10a).

Beneath the arc, on the other hand, the conditions recorded by the melt inclusions are indicative of melts equilibrating over a very broad range of P–T conditions, extending to greater depths and higher absolute temperatures than the anhydrous back-arc melting triangle (Figs 7 and 10). Considering possible cooling during melting, the arc melts could be traced back along an adiabatic melting path to mantle of $T_p \sim 1400$–$1450°C$ (Fig. 10). Melting paths beneath arcs, however, may not be adiabatic if melts or partially molten sources migrate upwards and increase in temperature through the lower half of the mantle wedge (e.g. Grove *et al.*, 2006). Melting-induced cooling could thus be offset by the inverted geotherm in the lower half of the wedge, particularly if the volume of the mantle experiencing melting is small relative to the thermal reservoir of the mantle (Kelley *et al.*, 2006). Small parcels of ascending melt or partially molten mantle could equilibrate thermally with the progressively hotter mantle through which they rise, thus experiencing non-adiabatic heating, instead of cooling, during ascent and melting. The melt temperature would thus be fixed by the mantle temperature up to the maximum T in the hot core of the wedge, which would reflect the conditions of last equilibration of the arc melts with the arc mantle. In contrast to back-arc melting, which is driven by spreading and mantle upwelling, melting and melt equilibration beneath the arc may occur largely within the hot, central portion of the mantle wedge. When considering the average P–T conditions recorded by melts from each island (see Table 2), arc

Table 2: Average pressures and temperatures of equilibration of Mariana melts

Volcano or region	Av. T (°C)	SD	$T - T_o$ (°C)	Av. P (GPa)	SD
Guguan	1360	24	−39	1·9	0·3
Pagan	1343	31	−12	1·6	0·1
Agrigan	1365	47	−57	2·2	0·4
Sarigan	1208	0	−81	1·0	0·0
Mariana Trough	1273	22	+31	0·9	0·1

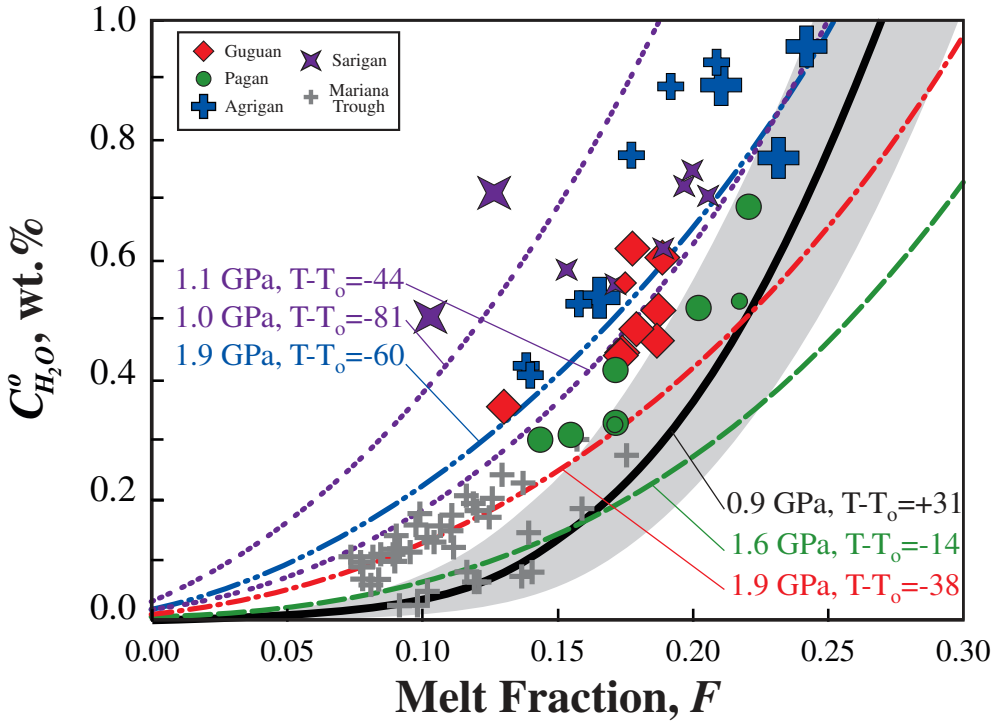

Fig. 11. Plot of $C^o_{H_2O}$ vs melt fraction (F) in Mariana arc and trough melts, incorporating various melting models. The modeled data points and symbols are the same as those shown in Fig. 6. The curves shown are outputs of variations of equation (4), using coefficients for the fertile and refractory cases. The pressures and temperatures input into each model are shown in Fig. 9 and are provided in Table 2. The thick, continuous black curve describes melting for the average P–T conditions of the Mariana Trough, using coefficients for the fertile case ($T - T_o = +31$). The shaded region surrounding this curve represents an uncertainty of ± 20°C on the fertile solidus. Models for the arc use coefficients for the refractory case. Arc model melting curves are shown for average P–T conditions of Pagan island (dashed curve; $T - T_o = -14$), Guguan island (dash–dot curve; $T - T_o = -38$), Agrigan island (dash–double-dot curve; $T - T_o = -60$), and the two distinct samples from Sarigan island (triple dotted curves; $T - T_o = -81$ and -44).

melting conditions are actually consistent with a maximum wedge core temperature of 1350°C or cooler (Fig. 10a).

Melting in the Mariana system

Although the thermobarometric results make some sense with respect to the physical arc and back-arc melting regimes (Fig. 7), they stand in apparent disagreement with the inferences from the data arrays on the $C^o_{H_2O}$ vs F diagram (Fig. 6), which indicate lower productivity of hydrous melting (i.e. lower $dF/dC^o_{H_2O}$) suggestive of cooler temperatures beneath the arc than the back-arc. Resolving this apparent contradiction requires an integrated examination of the factors controlling melt formation and productivity in the Mariana system, including pressure, temperature, and the peridotite fertility appropriate to this system. To develop a comprehensive view of the conditions of melting, the role of H_2O, and the influences over the form of the melting function for each location in the Mariana system, we combined our thermobarometric calculations with the fertile and refractory parameterizations of hydrous melting [e.g. equation (4)]. For the Mariana Trough, we use the fertile case, appropriate for MORB sources; for the Mariana arc, we use the refractory case to account for the increased depletion of the Mariana arc mantle relative to the Mariana Trough (see above). These choices utilize the best available constraints on solidi and melt productivities for fertile and comparatively depleted natural peridotite, and are intended to reflect the general characteristics of melting variably depleted mantle sources. We emphasize that the precise fertilities that apply to the mantle beneath the Mariana arc and trough are subject to debate. Those used here were chosen to illustrate the important first-order contrast between melting of fertile vs refractory lherzolite on melt productivity and on the form of the wet melting function.

Figure 11 shows the model melting curves output by equation (4) as described above, calculated for each location using P–T conditions determined from melt thermobarometry. For each island and for the whole Mariana Trough, pressures and temperatures given by each modeled glass were averaged (Table 2; Fig. 10a) to give a mean P–T condition for each location. In the case of Sarigan, where two samples yielded two distinct sets of P–T

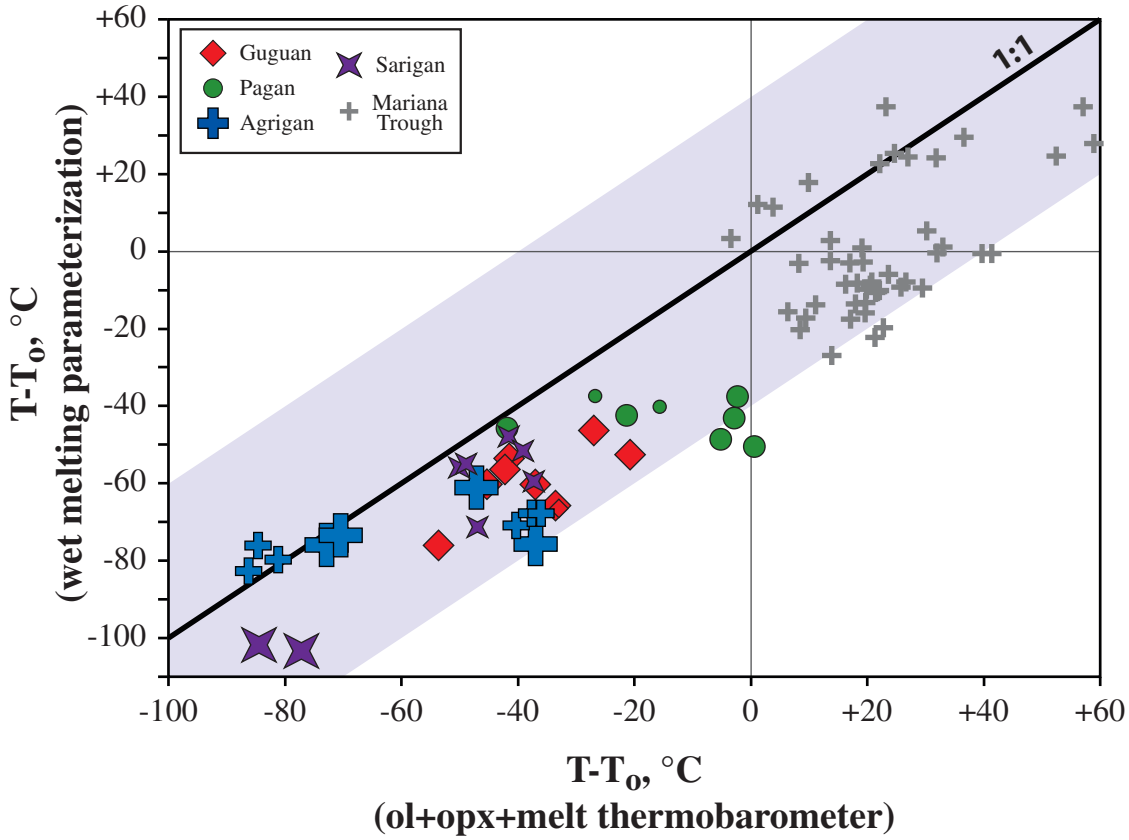

Fig. 12. Plot of $T - T_o$ derived from two independent methods. The *x*-axis represents $T - T_o$ calculated relative to fertile (Mariana Trough) or refractory (arc islands) peridotite solidi, using temperatures and pressures calculated using the ol + opx + melt thermobarometer of Lee *et al.* (2009). The *y*-axis represents $T - T_o$ calculated relative to fertile (Mariana Trough) or refractory (arc islands) peridotite solidi by solving equation (4) for $T - T_o$ (where $T_o = aP^2 + bP + c$), using the batch melting model results to supply F and $C^o_{H_2O}$ (see Electronic Appendix 4), and using the pressure derived from the Lee *et al.* (2009) model. The shaded region is ± 40°C from the 1:1 line, which is the quoted error on temperatures derived from the Lee *et al.* (2009) model.

conditions, the conditions for each sample were averaged separately. These calculations yield the amount of melting expected over a range of H_2O contents added to a fertile or refractory mantle wedge at the P–T conditions specified for each location. On the whole, the model curves are consistent with the modeled data points derived from TiO_2 systematics for the Mariana arc and trough. For example, the melts from Agrigan, Gugan, and Pagan islands show high equilibration pressures and temperatures (Figs 8 and 9), but also indicate temperatures below the anhydrous, refractory solidus ($T - T_o = -12$ to -60°C).

The P–T conditions indicated by these arc samples yield melting curves that broadly bracket many of the modeled data for these three islands, indicating that H_2O-fluxed melting of relatively refractory peridotite at the modeled P–T conditions is an appropriate mechanism to explain the data trends. In detail, however, the model curves for the arc melting conditions show melt productivities systematically higher than indicated by the arc data. This outcome may be a result of the DMM1 composition being too refractory relative to the true Mariana arc mantle source, or a refractory solidus that is too cold, or both. Lower productivities of a slightly more fertile peridotite would yield closer agreement between the arc data and the models. Nevertheless, the sense of variation among the arc volcanoes is accurately captured by the melting models, regardless of the exact melt productivities used, with Sarigan (SA93) as the coldest and least productive, and Pagan as the warmest and most productive. Without adjusting solidi or melt productivities, however, independent constraints on $T - T_o$ derived from the thermobarometry models (Lee *et al.*, 2009) and from equation (4) [solved for $T - T_o$, using the batch melting results to supply F and $C^o_{H_2O}$, and given P from the Lee *et al.*, (2009) model] are remarkably consistent. Figure 12 compares $T - T_o$ derived from both methods, and shows clear agreement, within error of the temperature model of Lee *et al.* (2009), although there is a systematic bias that may be resolved as discussed above with adjustments to solidi and/or melt productivities. Figure 12 also illustrates the consistency of the two models in resolving the strong temperature contrast beneath the arc (negative $T - T_o$)

relative to the back-arc basin (positive $T - T_o$), and among the arc islands, where $T - T_o$ decreases in the order Pagan > Guguan > Agrigan > Sarigan (SA93).

As a group, the melts from Sarigan indicate lower equilibration pressures than the other Mariana islands (~1 GPa), and the two inclusions from sample SA93, in particular, also record very low relative temperatures ($T - T_o = -80°C$; Fig. 9a), consistent with the lowest melting productivities among the samples examined here. For the Mariana Trough, the combination of lower equilibration pressures (~1 GPa) and a more fertile (i.e. colder; Fig. 9) solidus leads to super-solidus mean melts ($T - T_o = +31°C$) that are distinct from the sub-solidus mean melts of the Mariana arc. The model curve is not a good fit for many of the back-arc data, which suggests that the relevant solidus for the Mariana Trough may be ~10°C warmer than the fertile solidus (uncertainties on this solidus are ± ~20°C from 0 to 3·5 GPa; Hirschmann, 2000), but the important systematics are nonetheless clear. The inferences drawn from simple observations of slopes defined by the data trends in Figs 6 and 11 are inadequate to constrain melting conditions because the effects of pressure, temperature, and relevant peridotite fertility all combine to influence the shape of the melting function. We show here that the modeled data trends are consistent with arc melts equilibrating at higher temperatures and pressures than back-arc basin melts, and vary in melt fraction as a function of temperature, pressure, mantle fertility, and H_2O addition to the mantle source.

In summary, the relevant parameter for trends on the $C^o_{H_2O}$ vs F diagram is $T - T_o$, which is the relative temperature contrast with respect to the relevant solidus at a given pressure (e.g. relative to either the fertile or refractory solidus, as in Fig. 10a). This controls both the slope (particularly at negative $T - T_o$) and horizontal translation of the melting curves on the $C^o_{H_2O}$ vs F diagram, both of which are measures of the wet melting productivity (i.e. $dF/dC^o_{H_2O}$). Knowledge of $T - T_o$, however, requires independent constraints on the absolute P and T of melting, obtained here through thermobarometry, as well as independent constraints on the position of the anhydrous solidus. The quantitative consistency between these independent approaches demonstrates the utility of this framework for describing the melting relationships defined by natural arc and back-arc samples. For back-arc basins, where mantle fertility largely reflects that of the ambient convecting upper mantle, and where mantle T_p largely controls the depth and extent of melting, the slope of melting trends on the $C^o_{H_2O}$ vs F diagram is an adequate proxy for wet melting productivity, which increases with the mean pressure of melting and T_p, as indicated in this study and previously (Kelley *et al.*, 2006). For arcs, the mantle composition could be either more refractory or more enriched than normal MORB mantle, as a result of, for example, the absence of back-arc spreading or ocean island basalt-like mantle sources (e.g. Woodhead *et al.*, 1993; Eiler *et al.*, 2005; Pearce *et al.*, 2005), and the mantle may begin to melt near the slab, at higher pressures than it would melt under drier conditions, driven by a high water flux from below. This drives significant melting at temperatures below the dry solidus, but with smaller increases in the amount of melting per unit of added water than occurs beneath back-arcs, particularly if the arc mantle is more refractory. We thus expect that, as more water data are produced for arc systems, many arcs will define steeper slopes on $C^o_{H_2O}$ vs F diagrams, with potentially lower average F, than back-arc basins. Recent work examining wet melting systematics for the Kamchatka, Central America, and Mexican arcs appear to substantiate this prediction (Portnyagin *et al.*, 2007; Johnson *et al.*, 2009).

CONCLUSIONS

The integrated approach developed here for describing the conditions of melting in the Mariana system predicts that the Mariana arc melts (excluding those from Sarigan) have equilibrated at greater depths (50–90 km), from more refractory mantle, and at higher absolute temperatures (>1300°C) and water contents ($C^o_{H_2O}$ > 2000 ppm) than back-arc basin melts from the Mariana Trough. Nonetheless, most of the melts beneath the arc are generated at temperatures below the dry solidus, and so by a less productive wet melting process than beneath the back-arc. The contrast in the arc and back-arc melting productivities reflects the different physical processes involved: low water concentrations within a dominantly spreading-driven upwelling system beneath the back-arc vs higher water concentrations within the hot, central portion of the comparatively stagnant mantle wedge beneath the arc. This does not exclude a significant component of dry melting beneath the arc, but our data range is too limited to explicitly define the low-H_2O ends of the arc melting trends and our thermobarometric approach relies on mean properties of the aggregate melts rather than the discrete melts that may exist within the mantle. However, the quantitative constraints on the pressures and temperatures of melting presented here allow us to describe the wet melting process within the Mariana arc–back-arc system in a self-consistent way, as a function of the combined effects of the geothermal gradient, mantle fertility, and the magnitude of H_2O addition to the mantle wedge, providing a useful framework for the examination of other subduction systems.

FUNDING

This work was supported in part by two grants from the National Science Foundation (grant numbers OCE #0001897 to T.P., OCE #0623238 to K.K.) and a

National Science Foundation Graduate Research Fellowship, a Carnegie Fellowship, and a University of Rhode Island ADVANCE fellowship to K.K.

ACKNOWLEDGEMENTS

Thanks go to Fred Anderson for his great generosity in sharing his Mariana arc scoria collection with us. Many thanks also go to Neel Chatterjee at MIT and Chris Hadidiacos at GL/CIW for essential assistance with electron microprobe operations, and to Jianhua Wang at DTM/CIW for essential support with SIMS analyses. Marc Hirschmann, Charlie Langmuir, Rich Katz, Mark Behn and Liz Cottrell provided inspirational and progressive discussion over the course of this work. We are grateful to Paul Asimow, Jon Blundy, Julian Pearce and Paul Wallace for detailed, thoughtful and constructive reviews.

SUPPLEMENTARY DATA

Supplementary data for this paper are available at *Journal of Petrology* online.

REFERENCES

Anderson, A. T., Jr (1979). Water in some hypersthenic magmas. *Journal of Geology* **87**, 509–531.

Anderson, A. T., Jr (1982). Parental basalts in subduction zones: Implications for continental evolution. *Journal of Geophysical Research* **87**, 7047–7060.

Antignano, A. & Manning, C. E. (2008). Rutile solubility in H_2O, H_2O–SiO_2, and H_2O–$NaAlSi_3O_8$ fluids at 0·7–2·0 GPa and 700–1000°C: Implications for mobility of nominally insoluble elements. *Chemical Geology* **255**, 283–293, doi:10.1016/j.chemgeo.2008.07.001.

Asimow, P. D., Hirschmann, M. M. & Stolper, E. M. (1997). An analysis of variations in isentropic melt productivity. *Philosophical Transactions of the Royal Society of London, Series A* **355**, 255–281.

Baker, D. R. (2008). The fidelity of melt inclusions as records of melt composition. *Contributions to Mineralogy and Petrology* **156**, 377–395, doi:10.1007/s00410-008-0291-3.

Baker, D. R., Freda, C., Brooker, R. A. & Scarlato, P. (2005). Volatile diffusion in silicate melts and its effects on melt inclusions. *Annals of Geophysics* **48**, 699–717.

Baker, M. B. & Stolper, E. M. (1994). Determining the composition of high-pressure mantle melts using diamond aggregates. *Geochimica et Cosmochimica Acta* **58**, 2811–2827, doi:10.1016/0016-7037(94)90116-3.

Baker, M. B., Hirschmann, M. M., Ghiorso, M. S. & Stolper, E. (1995). Compositions of near-solidus peridotite melts from experiments and thermodynamic calculation. *Nature* **375**, 308–311.

Banks, N. G., Koyanagi, R. Y., Sinton, J. M. & Honma, K. T. (1984). The eruption of Mount Pagan volcano, Mariana islands, 15 May 1981. *Journal of Volcanology and Geothermal Research* **22**, 225–269.

Benjamin, E., Plank, T., Wade, J. A., Kelley, K. A., Hauri, E. H. & Alvarado, G. E. (2007). High water contents in basaltic magmas from Irazú Volcano, Costa Rica. *Journal of Volcanology and Geothermal Research* **168**, 68–92, doi:10.1016/j.jvolgeores.2007.08.008.

Blundy, J., Cashman, K. & Humphreys, M. (2006). Magma heating by decompression-driven crystallization beneath andesite volcanoes. *Nature* **443**, 76–80, doi:10.1038/nature05100.

Cervantes, P. & Wallace, P. J. (2003). Role of H_2O in subduction-zone magmatism: New insights from melt inclusions in high-Mg basalts from central Mexico. *Geology* **31**, 235–238.

Conder, J. A., Wiens, D. A. & Morris, J. D. (2002). On the decompression melting structure at volcanic arcs and back-arc spreading centers. *Geophysical Research Letters* **29**, 1–4.

Davies, J. H. & Stevenson, D. J. (1992). Physical model of source region of subduction zone volcanics. *Journal of Geophysical Research* **97**, 2037–2070.

Dixon, J. E. & Stolper, E. (1995). An experimental study of water and carbon dioxide solubilities in mid-ocean ridge basaltic liquids. Part II. Applications to degassing. *Journal of Petrology* **36**, 1633–1646.

Dixon, T. H. & Batiza, R. (1979). Petrology and geochemistry of recent lavas in the northern Marianas. *Contributions to Mineralogy and Petrology* **70**, 167–181.

Eiler, J. M., Carr, M. J., Reagan, M. K. & Stolper, E. M. (2005). Oxygen isotope constraints on the sources of Central American arc lavas. *Geochemistry, Geophysics, Geosystems* **6**, Q07007, doi:10.1029/2004GC000804.

Elliott, T., Plank, T., Zindler, A., White, W. M. & Bourdon, B. (1997). Element transport from slab to volcanic front at the Mariana arc. *Journal of Geophysical Research* **102**, 14991–15019.

England, P., Engdahl, E. R. & Thatcher, W. (2004). Systematic variation in the depths of slabs beneath arc volcanoes. *Geophysical Journal International* **156**, 377–408, doi:10.1111/j.1365-246X.2003.02132.x.

Fryer, P., Sinton, J. M. & Philpotts, J. A. (1981). Basaltic glasses from the Mariana Trough. In: Hussong, D. M. & Uyeda, S. (eds) *Initial Reports of the Deep Sea Drilling Project, Vol. 60*. Washington, DC: US Government Publishing Office, pp. 601–609.

Gaetani, G. A. & Grove, T. L. (1998). The influence of water on melting of mantle peridotite. *Contributions to Mineralogy and Petrology* **131**, 323–246.

Gaetani, G. A. & Grove, T. L. (2003). Experimental constraints on melt generation in the mantle wedge. In: Eiler, J. M. (ed.) *Inside the Subduction Factory. Geophysical Monograph, American Geophysical Union* **138**, 107–134.

Gerya, T. V. & Yuen, D. A. (2003). Rayleigh–Taylor instabilities from hydration and melting propel 'cold plumes' at subduction zones. *Earth and Planetary Science Letters* **212**, 47–62.

Gribble, R. F., Stern, R. J., Bloomer, S. H., Stuben, D., O'Hearn, T. & Newman, S. (1996). MORB mantle and subduction components interact to generate basalts in the southern Mariana Trough back-arc basin. *Geochimica et Cosmochimica Acta* **60**, 2153–2166.

Gribble, R. F., Stern, R. J., Newman, S., Bloomer, S. H. & O'Hearn, T. (1998). Chemical and isotopic composition of lavas from the Northern Mariana Trough: Implications for magmagenesis in back-arc basins. *Journal of Petrology* **39**, 125–154.

Grove, T. L., Parman, S. W., Bowring, S. A., Price, R. C. & Baker, M. B. (2002). The role of an H_2O-rich fluid component in the generation of primitive basaltic andesites and andesites from the Mt. Shasta region, N California. *Contributions to Mineralogy and Petrology* **142**, 375–396.

Grove, T. L., Chatterjee, N., Parman, S. W. & Médard, E. (2006). The influence of H_2O on mantle wedge melting. *Earth and Planetary Science Letters* **249**, 74–89, doi:10.1016/j.epsl.2006.06.043.

Hall, P. S. & Kincaid, C. (2001). Diapiric flow at subduction zones: A recipe for rapid transport. *Science* **292**, 2472–2475.

Hauri, E. (2002*a*). SIMS investigations of volatiles in silicate glasses, 1: calibration, sensitivity and comparisons with FTIR. *Chemical Geology* **183**, 99–114.

Hauri, E. H. (2002*b*). SIMS investigations of volatiles in silicate glasses, 2: isotopes and abundances in Hawaiian melt inclusions. *Chemical Geology* **183**, 115–141.

Hawkins, J. W., Lonsdale, P. F., Macdougall, J. D. & Volpe, A. M. (1990). Petrology of the axial ridge of the Mariana Trough backarc spreading center. *Earth and Planetary Science Letters* **100**, 226–250.

Hirschmann, M. M. (2000). Mantle solidus: Experimental constraints and the effects of peridotite composition. *Geochemistry, Geophysics, Geosystems* **1**, doi:10.1029/2000GC000070.

Hirschmann, M. M., Baker, M. B. & Stolper, E. M. (1998). The effect of alkalis on the silica content of mantle-derived melts. *Geochimica et Cosmochimica Acta* **62**, 883–902, doi:10.1016/S0016-7037(98)00028-3.

Hirschmann, M. M., Asimow, P. D., Ghiorso, M. S. & Stolper, E. (1999). Calculation of peridotite partial melting from thermodynamic models of minerals and melts. III. Controls on isobaric melt production and the effect of water on melt production. *Journal of Petrology* **40**, 831–851.

Hirschmann, M. M., Aubaud, C. & Withers, A. C. (2005). Storage capacity of H_2O in nominally anhydrous minerals in the upper mantle. *Earth and Planetary Science Letters* **236**, 167–181, doi:10.1016/j.epsl.2005.04.022.

Hirschmann, M. M., Tenner, T., Aubaud, C. & Withers, A. C. (2009). Dehydration melting of nominally anhydrous mantle: The primacy of partitioning. *Physics of the Earth and Planetary Interiors* **176**, 54–68, doi:10.1016/j.pepi.2009.04.001.

Johnson, E. R., Wallace, P. J., Delgado Granados, H., Manea, V. C., Kent, A. J. R., Bindeman, I. N. & Donegan, C. S. (2009). Subduction-related volatile recycling and magma generation beneath central Mexico: Insights from melt inclusions, oxygen isotopes and geodynamic models. *Journal of Petrology* **50**, 1729–1764, doi:10.1093/petrology/egp051.

Johnson, K. T. M. (1998). Experimental determination of partition coefficients for rare earth and high-field-strength elements between clinopyroxene, garnet, and basaltic melt at high pressures. *Contributions to Mineralogy and Petrology* **133**, 60–68.

Katz, R. F., Spiegelman, M. & Langmuir, C. H. (2003). A new parameterization of hydrous mantle melting. *Geochemistry, Geophysics, Geosystems* **4**, doi:10.1029/2002GC000433.

Kelemen, P. B., Yogodzinski, G. M. & Scholl, D. W. (2003). Along-strike variation in the Aleutian island arc: Genesis of high Mg# andesite and implications for continental crust. In: Eiler, J. M. (ed.) *Inside the Subduction Factory. Geophysical Monograph, American Geophysical Union* **138**, 223–276.

Kelley, K. A. & Cottrell, E. (2009). Water and the oxidation state of subduction zone magmas. *Science* **325**, 605–607, doi:10.1126/science.1174156.

Kelley, K. A., Plank, T., Grove, T. L., Stolper, E. M., Newman, S. & Hauri, E. H. (2006). Mantle melting as a function of water content beneath back-arc basins. *Journal of Geophysical Research* **111**, B09208, doi:10.1029/2005JB003732.

Kent, A. J. R., Peate, D. W., Newman, S., Stolper, E. & Pearce, J. A. (2002). Chlorine in submarine glasses from the Lau Basin: seawater contamination and constraints on the composition of slab-derived fluids. *Earth and Planetary Science Letters* **202**, 361–377.

Kincaid, C. & Hall, P. S. (2003). Role of back-arc spreading in circulation and melting at subduction zones. *Journal of Geophysical Research* **108**, doi:10.1029/2001JB001174.

Klein, E. M. & Langmuir, C. H. (1987). Global correlations of ocean ridge basalt chemistry with axial depth and crustal thickness. *Journal of Geophysical Research* **92**, 8089–8115.

Kushiro, I. (1972). Effect of water on the composition of magmas formed at high pressures. *Journal of Petrology* **13**, 311–334.

Kushiro, I., Syono, Y. & Akimoto, S. (1968). Melting of a peridotite nodule at high pressures and high water pressures. *Journal of Geophysical Research* **73**, 6023–6029.

Langmuir, C. H., Klein, E. M. & Plank, T. (1992). Petrological systematics of mid-ocean ridge basalts: Constraints on melt generation beneath ocean ridges. In: Phipps Morgan, J., Blackman, D. K. & Sinton, J. M. (eds) *Mantle Flow and Melt Generation at Mid-Ocean Ridges. Geophysical Monograph, American Geophysical Union* **71**, 183–280.

Langmuir, C. H., Bézos, A., Escrig, S. & Parman, S. W. (2006). Chemical systematics and hydrous melting of the mantle in back-arc basins. In: Christie, D. M. & Fisher, C. R. (eds) *Back-arc Spreading Systems: Geological, Biological, Chemical, and Physical Interactions. Geophysical Monograph, American Geophysical Union* **166**, 87–146.

Larson, E. E., Reynolds, R. L., Merrill, R., Levi, S., Ozima, M., Aoki, Y., Kinoshita, H., Zasshu, S., Kawai, N., Nakajima, T. & Horooka, K. (1974). Major-element petrochemistry of some extrusive rocks from the volcanically active Mariana islands. *Bulletin of Volcanology* **38**, 361–377.

Lee, C.-T. A., Luffi, P., Plank, T., Dalton, H. & Leeman, W. P. (2009). Constraints on the depths and temperatures of basaltic magma generation on Earth and other terrestrial planets using new thermobarometers. *Earth and Planetary Science Letters* **279**, 20–33, doi:10.1016/j.epsl.2008.12.020.

Morris, J. D., Leeman, W. P. & Tera, F. (1990). The subducted component in island arc lavas; constraints from B–Be isotopes and Be systematics. *Nature* **344**, 31–36.

Newman, S. & Lowenstern, J. B. (2002). VolatileCalc: a silicate melt–H_2O–CO_2 solution model written in Visual Basic for Excel. *Computers and Geosciences* **28**, 597–604.

Newman, S., Stolper, E. & Stern, R. J. (2000). H_2O and CO_2 in magmas from the Mariana arc and back-arc systems. *Geochemistry, Geophysics, Geosystems* **1**, doi:10.1029/1999GC000027.

Nielsen, R. L., Crum, J., Bourgeois, R., Hascall, K., Forsythe, L. M., Fisk, M. & Christie, D. M. (1995). Melt inclusions in high-An plagioclase from the Gorda Ridge: an example of the local diversity of MORB parent magmas. *Contributions to Mineralogy and Petrology* **122**, 34–50, doi:10.1007/s004100050111.

Parman, S. & Grove, T. L. (2004). Harzburgite melting with and without H_2O: experimental data and predictive modeling. *Journal of Geophysical Research* **109**, doi:10.1029/2003JB002566.

Parman, S. W., Grove, T. L., Kelley, K. A. & Plank, T. (2010). Estimates of along-arc H_2O variations in Mariana arc magmas using fractionation paths. *Journal of Petrology* (submitted).

Pearce, J. & Parkinson, I. J. (1993). Trace element models for mantle melting: Application to volcanic arc petrogenesis. In: Prichard, H. M., Alabaster, T., Harris, N. B. W. & Nears, C. R. (eds) *Magmatic Processes and Plate Tectonics. Geological Society, London, Special Publications* **76**, 373–403.

Pearce, J. A. (2005). Mantle preconditioning by melt extraction during flow: theory and petrogenetic implications. *Journal of Petrology* **46**, 973–997, doi:10.1093/petrology/egi007.

Pearce, J. A., Stern, R. J., Bloomer, S. H. & Fryer, P. (2005). Geochemical mapping of the Mariana arc–basin system: Implications for the nature and distribution of subduction components. *Geochemistry, Geophysics, Geosystems* **6**, Q07006, doi:10.1029/2004GC000895.

Plank, T. (2005). Constriants from thorium/lanthanum on sediment recycling at subduction zones and the evolution of the continents. *Journal of Petrology* **46**, 921–944, doi:10.1093/petrology/egi005.

Plank, T. & Langmuir, C. H. (1988). An evaluation of the global variations in the major element chemistry of arc basalts. *Earth and Planetary Science Letters* **90**, 349–370.

Plank, T. & Langmuir, C. H. (1993). Tracing trace elements from sediment to volcanic output at subduction zones. *Nature* **362**, 739–742.

Portnyagin, M., Hoernle, K., Plechov, P., Mironov, N. & Khubunaya, S. (2007). Constraints on mantle melting and composition and nature of slab components in volcanic arcs from volatiles (H_2O, S, Cl, F) and trace elements in melt inclusions from the Kamchatka arc. *Earth and Planetary Science Letters* **255**, 53–69, doi:10.1016/j.epsl.2006.12.005.

Pozgay, S. H., Wiens, D. A., Conder, J. A., Shiobara, H. & Sugioka, H. (2009). Seismic attenuation tomography of the Mariana subduction system: implications for thermal structure, volatile distribution, and slow spreading dynamics. *Geochemistry, Geophysics, Geosystems* **10**, doi:10.1029/2008GC002313.

Roggensack, K. (2001). Unraveling the 1974 eruption of Fuego volcano (Guatemala) with small crystals and their young melt inclusions. *Geology* **29**, 911–914.

Roggensack, K., Hervig, R. L., McKnight, S. B. & Williams, S. N. (1997). Explosive basaltic volcanism from Cerro Negro volcano: Influence of volatiles on eruptive style. *Science* **277**, 1639–1642.

Saal, A. E., Hart, S. R., Shimizu, N., Hauri, E. H. & Layne, G. D. (1998). Pb isotopic variability in melt inclusions from oceanic island basalts, Polynesia. *Science* **282**, 1481–1484.

Saal, A. E., Hauri, E. H., Langmuir, C. H. & Perfit, M. R. (2002). Vapour undersaturation in primitive mid-ocean-ridge basalt and the volatile content of Earth's upper mantle. *Nature* **419**, 451–455.

Sadofsky, S. J., Portnyagin, M., Hoernle, K. & van den Bogaard, P. (2008). Subduction cycling of volatiles and trace elements through the Central American volcanic arc: evidence from melt inclusions. *Contributions to Mineralogy and Petrology* **155**, 433–456, doi:10.1007/s00410-007-0251-3.

Salters, V. J. M. & Stracke, A. (2004). Composition of the depleted mantle. *Geochemistry, Geophysics, Geosystems* **5**, doi:10.1029/2003GC000597.

Shaw, A. M., Hauri, E. H., Fischer, T. P., Hilton, D. R. & Kelley, K. A. (2008). Hydrogen isotopes in Mariana arc melt inclusions: implications for subduction dehydration and the deep-Earth water cycle. *Earth and Planetary Science Letters* **275**, 138–145, doi:10.1016/j.epsl.2008.08.015.

Sisson, T. W. & Grove, T. L. (1993*a*). Experimental investigations of the role of H_2O in calc-alkaline differentiation and subduction zone magmatism. *Contributions to Mineralogy and Petrology* **113**, 143–166, doi:10.1007/BF00283225.

Sisson, T. W. & Grove, T. L. (1993*b*). Temperatures and H_2O contents of low MgO high-alumina basalts. *Contributions to Mineralogy and Petrology* **113**, 167–184, doi:10.1007/BF00283226.

Sisson, T. W. & Layne, G. D. (1993). H_2O in basalt and basaltic andesite glass inclusions from four subduction-related volcanoes. *Earth and Planetary Science Letters* **117**, 619–635.

Smith, P. M. & Asimow, P. D. (2005). Adiabat_1ph: A new public front-end to the MELTS, pMELTS, and pHMELTS models. *Geochemistry, Geophysics, Geosystems* **6**, doi:10.1029/2004GC000816.

Sobolev, A. V. & Chaussidon, M. (1996). H_2O concentrations in primary melts from supra-subduction zones and mid-ocean ridges: Implications for H_2O storage and recycling in the mantle. *Earth and Planetary Science Letters* **137**, 45–55, doi:10.1016/0012-821X(95)00203-O.

Sobolev, A. V. & Shimizu, N. (1993). Ultra-depleted primary melt included in an olivine from the Mid-Atlantic Ridge. *Nature* **363**, 151–154.

Stern, R. J. (1979). On the origin of andesite in the northern Mariana island arc: Implications from Agrigan. *Contributions to Mineralogy and Petrology* **68**, 207–219.

Stolper, E. (1982). Water in silicate glasses: An infrared spectroscopic technique. *Contributions to Mineralogy and Petrology* **81**, 1–17.

Stolper, E. & Newman, S. (1994). The role of water in the petrogenesis of Mariana Trough magmas. *Earth and Planetary Science Letters* **121**, 293–325.

Takahashi, N., Kodaira, S., Klemperer, S. L., Tatsumi, Y., Kaneda, Y. & Suyehiro, K. (2007). Crustal structure and evolution of the Mariana intra-oceanic island arc. *Geology* **35**, 203–206, doi:10.1130/G23212A.

Tamaki, K. (1985). Two modes of back-arc spreading. *Geology* **13**, 475–478.

Taylor, B. & Martinez, F. (2003). Back-arc basin basalt systematics. *Earth and Planetary Science Letters* **210**, 481–497.

Tera, F., Brown, L. D., Morris, J. D., Sacks, S., Klein, J. & Middleton, J. (1986). Sediment incorporation in island-arc magmas: Inference from ^{10}Be. *Geochimica et Cosmochimica Acta* **50**, 535–550.

Wade, J. A., Plank, T., Melson, W. G., Soto, G. J. & Hauri, E. H. (2006). The volatile content of magmas from Arenal volcano, Costa Rica. *Journal of Volcanology and Geothermal Research* **157**, 94–120, doi:10.1016/j.jvolgeores.2006.03.045.

Walker, J. A., Roggensack, K., Patino, L. C., Cameron, B. I. & Otoniel, M. (2003). The water and trace element contents of melt inclusions across an active subduction zone. *Contributions to Mineralogy and Petrology* **146**, 62–77, doi:10.1007/s00410-003-0482-x.

Wallace, P. J. (2005). Volatiles in subduction zone magmas: concentrations and fluxes based on melt inclusion and volcanic gas data. *Journal of Volcanology and Geothermal Research* **140**, 217–240, doi:10.1016/j.jvolgeores.2004.07.023.

Walter, M. J. (1998). Melting of garnet peridotite and the origin of komatiite and depleted lithosphere. *Journal of Petrology* **39**, 29–60.

Wang, K., Plank, T., Walker, J. D. & Smith, E. I. (2002). A mantle melting profile across the Basin and Range, SW USA. *Journal of Geophysical Research* **107**, doi:10.1029/2001JB000209.

Wasylenki, L. E., Baker, M. B., Kent, A. J. R. & Stolper, E. M. (2003). Near-solidus melting of the shallow upper mantle: Partial melting experiments on depleted peridotite. *Journal of Petrology* **44**, 1163–1191.

Wiens, D. A., Kelley, K. A. & Plank, T. (2006). Mantle temperature variations beneath back-arc spreading centers inferred from seismology, petrology, and bathymetry. *Earth and Planetary Science Letters* **248**, 30–42, doi:10.1016/j.epsl.2006.04.011.

Wood, B. J. (2004). Melting of fertile peridotite with variable amounts of H_2O. In: Sparks, R. S. J. & Hawkesworth, C. J. (eds) *The State of the Planet: Frontiers and Challenges in Geophysics. Geophysical Monograph, American Geophysical Union* **150**, 69–80.

Woodhead, J. D. (1989). Geochemistry of the Mariana arc (western Pacific): Source composition and processes. *Chemical Geology* **76**, 1–24, doi:10.1016/0009-2541(89)90124-1.

Woodhead, J. D., Eggins, S. M. & Gamble, J. (1993). High field strength and transition element systematics in island arc and back-arc basin basalts: Evidence for multi-phase melt extraction and a depleted mantle wedge. *Earth and Planetary Science Letters* **114**, 491–504, doi:10.1016/0012-821X(93)90078-N.

Yoder, H. S. (1969). Calc-alkaline andesites: Experimental data bearing on the origin of their assumed characteristics. In: McBirney, A. R. (ed.) *Proceedings of the Andesite Conference*. State of Oregon, Department of Geology and Mineral Industries, Portland, OR, pp. 77–91.